The Astrophysical Journal, 912:95 (19pp), 2021 May 10 https://doi.org/10.3847/1538-4357/abee85

GRB 180418A: A Possibly Short Gamma-Ray Burst with a Wide-angle Outflow in a Faint Host Galaxy

A. Rouco Escorial[1], W. Fong[1], P. Veres[2], T. Laskar[3], A. Lien[4,5], K. Paterson[1], M. Lally[1], P. K. Blanchard[1], A. E. Nugent[1], N. R. Tanvir[6], D. Cornish[1], E. Berger[7], E. Burns[8,21], S. B. Cenko[8,9], B. E. Cobb[10], A. Cucchiara[11,12], A. Goldstein[13], R. Margutti[1], B. D. Metzger[14,18], P. Milne[16], A. Levan[17,15], M. Nicholl[19,20], and Nathan Smith[16]

[1] Center for Interdisciplinary Exploration and Research in Astrophysics (CIERA) and Department of Physics and Astronomy, Northwestern University, 1800 Sherman Avenue, Evanston, IL 60201, USA; alicia.rouco.escorial@northwestern.edu
[2] Center for Space Plasma and Aeronomic Research, University of Alabama in Huntsville, 320 Sparkman Drive, Huntsville, AL 35899, USA
[3] Department of Physics, University of Bath, Claverton Down, Bath, BA2 7AY, UK
[4] Center for Research and Exploration in Space Science and Technology (CRESST) and NASA Goddard Space Flight Center, Greenbelt, MD 20771, USA
[5] Department of Physics, University of Maryland, Baltimore County, 1000 Hilltop Circle, Baltimore, MD 21250, USA
[6] School of Physics and Astronomy, University of Leicester, University Road, Leicester, LE1 7RH, UK
[7] Center for Astrophysics |Harvard & Smithsonian, 60 Garden Street, Cambridge, MA 02138, USA
[8] NASA Goddard Space Flight Center, University of Maryland, Baltimore County, Greenbelt, MD 20771, USA
[9] Joint Space-Science Institute, University of Maryland, College Park, MD 20742, USA
[10] Department of Physics, The George Washington University, Washington, DC 20052, USA
[11] College of Marin, 120 Kent Avenue, Kentfield, CA 94904, USA
[12] University of the Virgin Islands, #2 Brewers Bay Road, Charlotte Amalie, 00802 USVI, USA
[13] Science and Technology Institute, Universities Space Research Association, Huntsville, AL 35805, USA
[14] Center for Computational Astrophysics, Flatiron Institute, 162 W. 5th Avenue, New York, NY 10011, USA
[15] Department of Physics and Columbia Astrophysics Laboratory, Columbia University, New York, NY 10027, USA
[16] University of Arizona, Steward Observatory, 933 N. Cherry Avenue, Tucson, AZ 85721, USA
[17] Department of Astrophysics/IMAPP, Radboud University, 6525 AJ Nijmegen, The Netherlands
[18] Department of Physics, University of Warwick, Coventry, CV4 7AL, UK
[19] Birmingham Institute for Gravitational Wave Astronomy and School of Physics and Astronomy, University of Birmingham, Birmingham B15 2TT, UK
[20] Institute for Astronomy, University of Edinburgh, Royal Observatory, Blackford Hill, EH9 3HJ, UK
Received 2020 December 17; revised 2021 March 2; accepted 2021 March 13; published 2021 May 10

Abstract

We present X-ray and multiband optical observations of the afterglow and host galaxy of GRB 180418A, discovered by Swift/BAT and Fermi/GBM. We present a reanalysis of the GBM and BAT data deriving durations of the prompt emission of $T_{90} \approx 2.56$ and 1.90 s, respectively. Modeling the Fermi/GBM catalog of 1405 bursts (2008–2014) in the hardness–T_{90} plane, we obtain a probability of ≈60% that GRB 180418A is a short-hard burst. From a combination of Swift/XRT and Chandra observations, the X-ray afterglow is detected to ≈38.5 days after the burst and exhibits a single power-law decline with $F_X \propto t^{-0.98}$. Late-time Gemini observations reveal a faint $r \approx 25.69$ mag host galaxy at an angular offset of $\approx 0\farcs16$. At the likely redshift range of $z \approx 1$–2.25, we find that the X-ray afterglow luminosity of GRB 180418A is intermediate between short and long gamma-ray bursts (GRBs) at all epochs during which there are contemporaneous data and that GRB 180418A lies closer to the $E_{\gamma,\mathrm{peak}}$–$E_{\gamma,\mathrm{iso}}$ correlation for short GRBs. Modeling the multiwavelength afterglow with the standard synchrotron model, we derive the burst explosion properties and find a jet opening angle of $\theta_j \gtrsim 9°$–14°. If GRB 180418A is a short GRB that originated from a neutron star merger, it has one of the brightest and longest-lived afterglows along with an extremely faint host galaxy. If, instead, the event is a long GRB that originated from a massive star collapse, it has among the lowest-luminosity afterglows and lies in a peculiar space in terms of the hardness–T_{90} and $E_{\gamma,\mathrm{peak}}$–$E_{\gamma,\mathrm{iso}}$ planes.

Unified Astronomy Thesaurus concepts: Gamma-ray transient sources (1853); Gamma-ray bursts (629)

1. Introduction

Gamma-ray bursts (GRBs) can be divided into two classes depending on their gamma-ray duration (T_{90}) and hardness of their γ-ray spectra: short-hard ($T_{90} \leqslant 2$ s) and long-soft ($T_{90} > 2$ s) bursts (Mazets et al. 1981; Norris et al. 1984; Dezalay et al. 1992; Kouveliotou et al. 1993). Multiwavelength observations of their synchrotron emission, or "afterglows" (e.g., Rees & Meszaros 1992; Meszaros & Rees 1993; van Paradijs et al. 2000), reveal specific information about the energetics, environments, and progenitor channels of these events, as well as the features of the highly relativistic jets that are expected to be launched by the central engine (Rhoads 1997; Panaitescu & Kumar 2002; Piran 2005). Since the launches of the Neil Gehrels Swift Observatory (Swift; Gehrels et al. 2004) and Fermi Gamma-ray Space Telescope (Fermi; GLAST Facility Science Team et al. 1999), more than 360 GRBs with known redshifts have been detected (Lien et al. 2016; von Kienlin et al. 2020). The joint power of both observatories has yielded not only an increase in the number of detected GRBs but also improved localizations of the events, allowing for secure associations to host galaxies.

Although the classification in terms of γ-ray hardness and T_{90} encompasses the large majority of GRBs, there are some events that defy clear classification under this scheme. The lack of supernova (SN) detections for some long-duration bursts (e.g., GRB 060505 and GRB 060614; Della Valle et al. 2006; Fynbo et al. 2006), the misidentification of host galaxies

[21] NASA Postdoctoral Fellow.

yielding to the incorrect classification of GRBs (e.g., GRB 060912A; Levan et al. 2007), the longer duration of some events with similar γ-ray hardness to the short GRB population (e.g., GRB 090607 and GRB 100816A; Barthelmy et al. 2009; D'Avanzo et al. 2014), and short-duration bursts with similar hardness and energy scales to those of the long GRBs (e.g., GRB 090426 and GRB 201015A; Antonelli et al. 2009; Markwardt et al. 2020) reveal the ambiguous nature of certain cases and the blurred lines between the GRB populations. Other metrics based on γ-ray information exist, such as adherence to the Yonetoku/Amati relation between the γ-ray peak energy and the isotropic-equivalent γ-ray energy (Amati et al. 2002; Yonetoku et al. 2004), and data-based probability schemes (Bromberg et al. 2013; Jespersen et al. 2020). In addition to the traditional GRB classification (short and long), a few studies (e.g., Horváth et al. 2006; de Ugarte Postigo et al. 2011) have proposed a third group of GRBs with intermediate durations, generally with T_{90} between 2 and 10 s. However, the existence of such a class has been a topic of debate since the existence of this third group depends on the instruments and the reference frames used (for an in-depth study see Kulkarni & Desai 2017).

As a class, long GRBs have been discovered up to $z \approx 9.4$ (e.g., Tanvir et al. 2009; Belczynski et al. 2010; Cucchiara et al. 2011; Salvaterra 2015), with median isotropic-equivalent energies of the order of $\approx 10^{51}$ erg (Frail et al. 2001; Berger et al. 2003; Gehrels et al. 2008; Laskar et al. 2014). The association of long GRBs with Type Ic SNe (e.g., Galama et al. 1998; Woosley & Bloom 2006; Hjorth & Bloom 2012), their small offsets from their host galaxies (Bloom et al. 2002b; Fruchter et al. 2006; Blanchard et al. 2016), their high circumburst densities of ≈ 0.1–$100\ \mathrm{cm}^{-3}$ (Panaitescu & Kumar 2002; Yost et al. 2003; Laskar et al. 2018), and their exclusive origins from star-forming galaxies (Wainwright et al. 2007) demonstrate that long GRBs result from the deaths of massive stars. On the other hand, short GRBs are detected at much lower redshifts, $z \approx 0.1$–2.2 (e.g., Fong et al. 2013; Berger et al. 2014), as a result of a combination of observational bias and the delay time distribution from their compact object binary progenitors (Selsing et al. 2018; Paterson et al. 2020). These events are less energetic, with observed median isotropic-equivalent energies of $\approx 10^{49}$ erg, and occur in environments with lower densities, i.e., $\approx 10^{-3}$–$10^{-2}\ \mathrm{cm}^{-3}$ (Nakar 2007; Nicuesa Guelbenzu et al. 2012; Berger 2014; Fong et al. 2015), commensurate with their larger offsets from their host galaxies (Fong & Berger 2013). The discovery of the first binary neutron star (BNS) merger gravitational-wave event, GW170817 (Abbott et al. 2017), in conjunction with a short gamma-ray burst GRB 170817A (Goldstein et al. 2017; Savchenko et al. 2017), provided direct evidence that at least some short GRBs originate from BNS mergers.

One of the most important parameters that can be gleaned from GRB afterglows is the jet opening angle, because their inference has direct consequences on the calculation of the true energy scale and rates of these events (e.g., Frail et al. 2001; Fong et al. 2015; Mandhai et al. 2018). For on-axis orientations, the jet opening angles can be determined from the detection of sudden steepenings in the broadband afterglow light curves (also called "jet breaks"; Piran 1999; Rhoads 1999; Sari et al. 1999; Panaitescu 2005), while limits on the jet opening angles can be inferred from the lack of jet breaks in the light curves. X-ray observations have played a leading role in these studies, thanks to the rapid X-ray detections and follow-up of most GRBs provided by Swift (Evans et al. 2007, 2009; Nysewander et al. 2009; Racusin et al. 2009). This facilitates not only the determination of the GRB afterglow decay rates but also a tightening of the constraints on the limits of the jet opening angles.

The relative brightness of long GRB afterglows (e.g., Bernardini et al. 2012; Del Vecchio et al. 2016) has led to the successful identification of jet breaks in their light curves, with opening angles of $< 10°$ (Frail et al. 2001; Racusin et al. 2009; Kann et al. 2010; Ryan et al. 2015; Goldstein et al. 2016). However, short GRB afterglows are generally fainter (e.g., Gehrels et al. 2008; Nysewander et al. 2009; Kann et al. 2010; Berger et al. 2013; Fong et al. 2015), making the identification of jet breaks in their light curves more challenging. For only a few short GRBs, jet opening angles have been measured between $\approx 2°$–$7°$ (e.g., Burrows et al. 2006; Soderberg et al. 2006; Fong et al. 2012; Troja et al. 2016; Lamb et al. 2019), while for the remaining events meaningful lower limits of $\gtrsim 4°$–$25°$ have been inferred at $\gtrsim 2$ days after the trigger (Fong et al. 2015; Jin et al. 2018). This may indicate that short GRBs have wider jets than their long-duration counterparts. So far, there is no clear mechanism to keep the jet collimated in the case of short GRBs (Sari et al. 1999; Mészáros & Rees 2001; Zhang et al. 2003).

In this paper, we present the multiwavelength afterglow monitoring of the potentially short GRB 180418A, spanning the X-ray and optical bands, and the discovery of its host galaxy. Our late-time Chandra detections of the X-ray afterglow of GRB 180418A extend up to ≈ 38.5 days after the trigger of the burst, representing one of the latest X-ray detections of a potential short GRB. In Section 2, we present the burst discovery and the Swift and Fermi data reanalysis classification of the burst. In Section 3, we introduce the multiwavelength afterglow observations and discovery of the host galaxy. We discuss the burst explosion properties and limits on the jet opening angle in Section 4. We compare our X-ray results to the Swift GRB population with known redshifts in Section 5. In Section 6, we discuss our results in the context of the short and long GRB populations. Finally, in Section 7, we summarize our conclusions.

Unless mentioned otherwise, all observations are reported in AB mag and have been corrected for Galactic extinction in the direction of the burst (Schlafly & Finkbeiner 2011). The cosmology employed in this paper is standard, with $H_0 = 69.6\ \mathrm{km\ s^{-1}\ Mpc^{-1}}$, $\Omega_{\mathrm{M}} = 0.286$, and $\Omega_{\mathrm{vac}} = 0.714$ (Bennett et al. 2014).

2. Burst Discovery and Classification

2.1. Initial Observations of GRB 180418A

GRB 180418A triggered the Burst Alert Telescope (BAT; Barthelmy et al. 2005) on board Swift at 06:44:06 UT on 2018 April 18, with an initially reported duration of ~ 1.5 s (D'Elia et al. 2018). Swift/BAT located the GRB to a refined position of R.A.(J2000) $= 11^{\mathrm{h}}20^{\mathrm{m}}31\overset{\mathrm{s}}{.}6$ and decl.(J2000) $= +24°55'28\overset{''}{.}9$ ($1\overset{'}{.}2$ radius uncertainty, 90% confidence; D'Elia et al. 2018) and revealed a single-peaked light curve with $T_{90} = 2.29 \pm 0.83$ s in the 15–350 keV energy band (Palmer et al. 2018). Additionally, GRB 180418A independently triggered and was detected by the Gamma-ray Burst Monitor (GBM; Meegan et al. 2009) aboard Fermi at 06:44:06.28 UT. The GBM light curve

consists of a single peak with an initially reported duration of $T_{90} \sim 2.5$ s in the 50–300 keV energy range (Bissaldi & Veres 2018).

The Swift/X-ray Telescope (XRT; Burrows et al. 2005) started the follow-up of GRB 180418A at $\delta t \approx 3.88 \times 10^3$ s (where δt represents the elapsed time since the BAT trigger). The slight delay of XRT observations with respect to the BAT detection was due to an observing constraint (D'Elia et al. 2018). An uncataloged X-ray source was discovered within the BAT position with an enhanced XRT position of R.A. (J2000) = $11^h20^m29^s.17$ and decl.(J2000) = $+24°55'59''.1$ ($1''.8$ radius uncertainty, 90% confidence; Goad et al. 2018) and identified as the X-ray afterglow of GRB 180418A. The afterglow of GRB 180418A was also detected and monitored in the optical band by ground-based facilities (see Section 3.2) and the Swift Ultraviolet/Optical Telescope (UVOT; Roming et al. 2005). UVOT detected the optical afterglow of GRB 180418A in the *white*, *u*, *uvw*1, and *uvm*2 filters (~19.0–19.5 mag at $\delta t \approx 3.5 \times 10^3$ s) but yielded nondetections in the *v*, *b*, and *uvw*2 filters (Siegel & D'Elia 2018).

In addition, radio observations of the field of GRB 180418A were performed using the Arcminute Microkelvin Imager (AMI; Zwart et al. 2008) Large Array at 15.5 GHz at $\delta t \approx 0.61$, 2.61, and 4.58 days. The radio afterglow was not detected to 3σ upper limits of $\gtrsim$99, $\gtrsim$81, and $\gtrsim$93 μJy, respectively (Bright et al. 2018).

2.2. Classification of GRB 180418A

The initial reported duration of GRB 180418A was T_{90} ~1.5–2.5 s (Bissaldi & Veres 2018; D'Elia et al. 2018). This makes the immediate classification of GRB 180418A ambiguous, given that the traditional division between short and long GRBs is placed at $T_{90} \sim 2$ s (e.g., Kouveliotou et al. 1993) and the exact location of this division is detector dependent (Bromberg et al. 2013; Lien et al. 2016; von Kienlin et al. 2020). Thus, to clarify the classification on this burst, we reanalyze the available Fermi/GBM and Swift/BAT data to determine both the duration and hardness ratio of GRB 180418A.

First, we analyze the Swift/BAT data of GRB 180418A, building on previous analyses reported by Palmer et al. (2018) and Becerra et al. (2019). The Swift/BAT catalog[22] reports a value of $T_{90} = 4.41 \pm 2.49$ s (15 − 350 keV), which is calculated using the standard setup of the BAT pipeline with a bin size of 4 ms (`batgrbproduct`; Lien et al. 2016). We reanalyzed the BAT light curve using two additional standard bin sizes of 16 and 64 ms, which give $T_{90} = 1.90 \pm 0.76$ s and 1.92 ± 0.72 s, respectively. Although the T_{90} values of all three bin choices are consistent with each other within the errors, we find that the duration and larger uncertainty obtained by the 4 ms binned light curve may be reflective of a potential weak tail emission following the initial peak of the light curve. In order to investigate this possibility, we create an image for $\delta t = 2.0$–4.0 s (15–350 keV) and detect the burst at $\sim 2.9\sigma$ level; therefore, we cannot rule out that the emission during this interval is due to a noise fluctuation.

Adopting a value of $T_{90} = 1.90 \pm 0.76$ s (16 ms bin), we calculate the GRB 180418A γ-ray fluence, f_γ, and hardness ratio following the same procedure used in the third Swift/BAT catalog (Lien et al. 2016). The spectrum corresponding to this T_{90} value is best fit by a single power-law model, $f(E) \propto E^{\Gamma_{\gamma,\mathrm{PL}}}$ (following the criteria in Sakamoto et al. 2011), with a photon index ($\Gamma_{\gamma,\mathrm{PL}}$) of ≈ -1.45. We measure a fluence of $f_\gamma = (2.85 \pm 0.20) \times 10^{-7}$ erg cm^{-2} (15 − 350 keV) and hardness ratio, defined as f_γ(50–100 keV)/f_γ(25–50 keV), of 1.47. In the context of the hardness–T_{90} plane for Swift/BAT GRBs (Lien et al. 2016), GRB 180418A appears to be a limiting case and close to the dividing threshold between short and long GRBs (although more recent machine-learning schemes based on the Swift/BAT catalog data alone classify GRB 180418A as "long"; Jespersen et al. 2020).

Next, we analyze the Fermi/GBM data, in which the T_{90} duration is typically measured in the 50–300keV energy range. The total flux, and thus T_{90} value, is obtained by using the `RMFIT` software to fit the background-subtracted spectrum for each time bin with an exponential cutoff power-law model (Gruber et al. 2014; Bhat et al. 2016) and a default temporal bin resolution of 64 ms (post-trigger resolution of the `CTIME` data type). Employing this method for GRB 180418A, we measure a single-peaked light curve with a duration of $T_{90} = 2.56 \pm 0.20$ s (1σ errors) in the 50–300 keV energy range and calculate the burst hardness over T_{90} as the ratio of deconvolved counts in the 50–300 keV to 10–50 keV energy ranges (von Kienlin et al. 2020). The resulting GBM hardness ratio of GRB 180418A is 0.728 ± 0.074. We also find that the best-fit model of the burst spectrum is a Comptonized model (`COMP`; an exponentially cutoff power law) characterized by $\Gamma_{\gamma,\mathrm{COMP}} = -1.20 \pm 0.15$ and a peak energy (E_{peak}) of 329 ± 123 keV (C-stat = 24.08 and dof = 16 using Castor statistics; Dorman et al. 2003; Ackermann et al. 2011). We derive $f_\gamma = 9.03 \times 10^{-7}$ erg cm^{-2} (10–1000 keV) over the interval duration. Adopting the parameters of the `COMP` model and fiducial redshift (z) values of 1.0 and 1.5, we obtain the 1−10,000 keV isotropic-equivalent γ-ray energy ($E_{\gamma,\mathrm{iso}}$) values of 2.71×10^{51} erg and 5.95×10^{51} erg, respectively.

We compare the values for GRB 180418A to those of the Fermi/GBM catalog comprising 1405 GRBs (2008 July 12 to 2014 July 11), which were analyzed in the same manner (Bhat et al. 2016; see Figure 1). We use the position of GRB 180418A in the hardness–T_{90} plane to quantify the probability that GRB 180418A is a long GRB (P_{long}). We fit the hardness–T_{90} distribution with two two-dimensional Gaussian components using the `mclust` package (Scrucca et al. 2016). The two components of each Gaussian correspond to the short and long GRB populations. Under this scheme, the probability P_{long} can be assigned to each burst based on its location in this plane (Figure 1). For GRB 180418A we obtain a probability $P_{\mathrm{long}} = 0.4$ (or, conversely, $P_{\mathrm{short}} = 0.6$). For comparison, we note that GRB 170817A, which was associated with GW170817, had a shorter duration but was slightly softer, with a value of $P_{\mathrm{long}} = 0.28$ (Goldstein et al. 2017; Figure 1). Based on the value of P_{long} for GRB 180418A and its similar position to GRB 170817A in the hardness–T_{90} plane, it is more plausible that GRB 180418A is likely a short-hard GRB.

3. Follow-up Observations of GRB 180418A

3.1. X-Ray Observations

3.1.1. Chandra Afterglow Detections

We used Chandra to obtain observations of the afterglow of GRB 180418A using the ACIS-S detector (Garmire et al. 2003)

[22] https://swift.gsfc.nasa.gov/results/batgrbcat/GRB180418A/web/GRB180418A.html

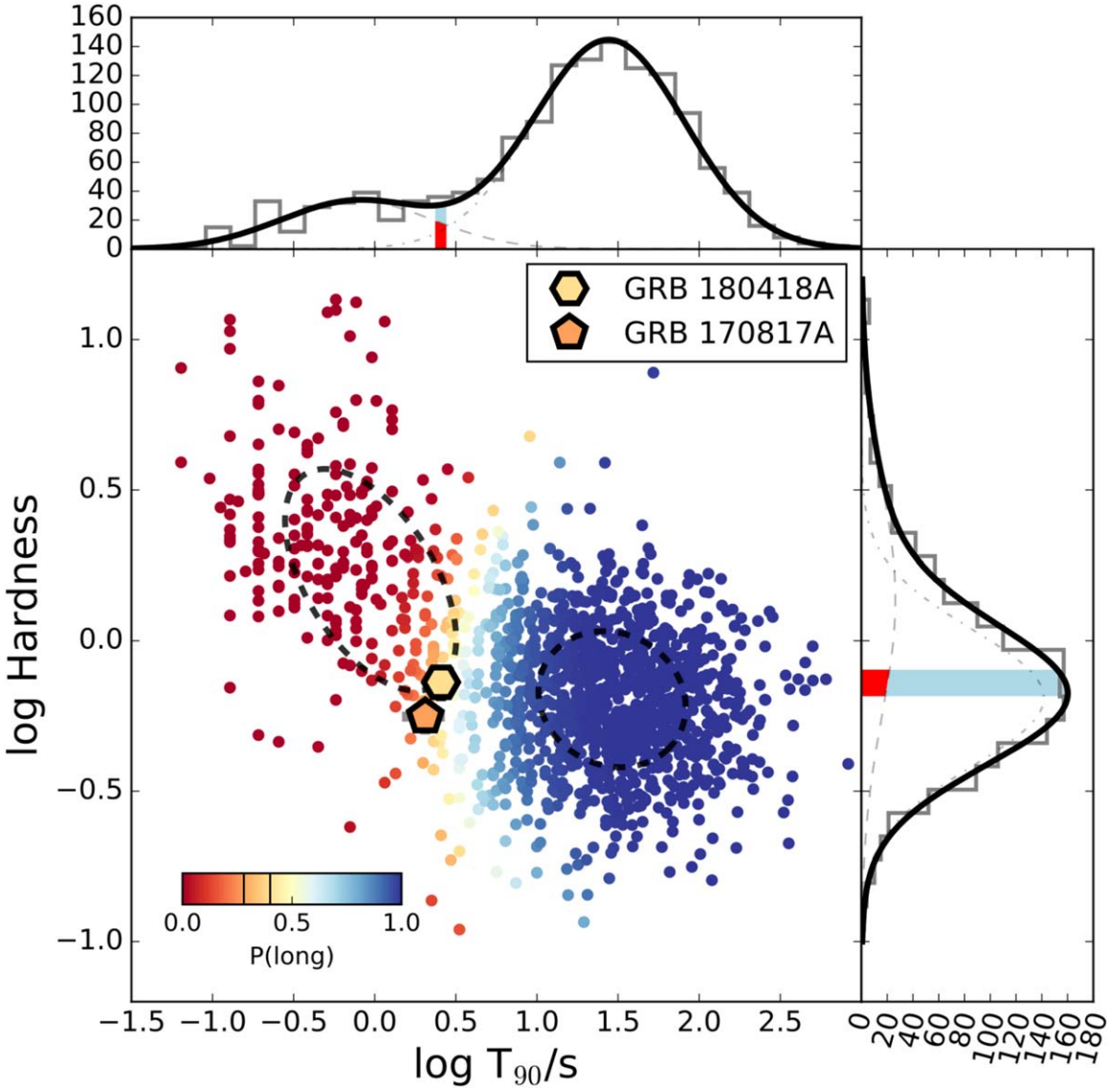

Figure 1. Hardness–T_{90} (observer frame) plane of 1405 bursts detected by Fermi/GBM (Bhat et al. 2016). The color scale from red to blue indicates the probability that a given event is a long GRB ($P_{\rm long}$), where a value of $P_{\rm long} = 0$ indicates a short GRB. In the projected histograms for each parameter (top and right), the contributions from the short (red) and long (light blue) GRB populations at the position of GRB 180418A are shown, containing the classification based only on either duration or hardness alone. We use two two-dimensional Gaussians to fit the distributions, where dashed-line ellipses correspond to 1σ confidence. The hexagon and pentagon indicate the locations of GRB 180418A and GRB 170817A, respectively. The position of each source has also been indicated with black lines in the probability color bar.

at $\delta t \approx 7.7$, 19.3, and 38.5 days (Figure 3; Program 19400201, PI: Fong). To reduce and analyze the data, we used the `CIAO` software package (v. 4.12; Fruscione et al. 2006) and the calibration database files (`caldb`; v. 4.9.0). We reprocessed the data to obtain new Level II event files and filtered each observation to exclude intervals of high background activity.

For the first Chandra observation at $\delta t \approx 7.7$ days (effective exposure time of $\sim$24 ks), we performed blind source detection using the `CIAO` routine `wavdetect` and detected the X-ray afterglow of GRB 180418A at a position of R.A. (J2000) = $11^{\rm h}20^{\rm m}29\overset{\rm s}{.}21$ and decl. (J2000) = $+24°55'59\overset{''}{.}21$, with a total positional uncertainty of $0\overset{''}{.}81$ (combining the afterglow centroid uncertainty of $0\overset{''}{.}091$ and the Chandra absolute astrometric uncertainty of $0\overset{''}{.}8$). The Chandra position is fully consistent with the enhanced XRT position (Figure 2). From the `wavdetect` output at the Chandra afterglow position, we obtain a total net source counts of 31 ± 6 in $\sim$24 ks and derive a source significance of 5σ. We analyzed the two remaining observations at 19.3 and 38.5 days in a similar manner; a blind search yields a nondetection and a detection of 6 ± 3 counts in 28 ks (2σ) at the position of the afterglow, respectively.

We also detect a neighboring X-ray source complex (hereafter X1) at an angular distance of $\sim 14\overset{''}{.}76$ from the afterglow, at R.A. (J2000) = $11^{\rm h}20^{\rm m}28\overset{\rm s}{.}61$ and decl. (J2000) = $+24°55'46\overset{''}{.}7$ (Figure 2). While our Chandra observations can separate these two sources, the contributions to the X-ray flux from both the afterglow and X1 are indistinguishable in XRT observations (Figure 2). Thus, we extract information from the position of X1 to model its X-ray spectral behavior and account for it in the XRT spectral analysis and derivation of the full X-ray afterglow light curve (Section 3.1.3).

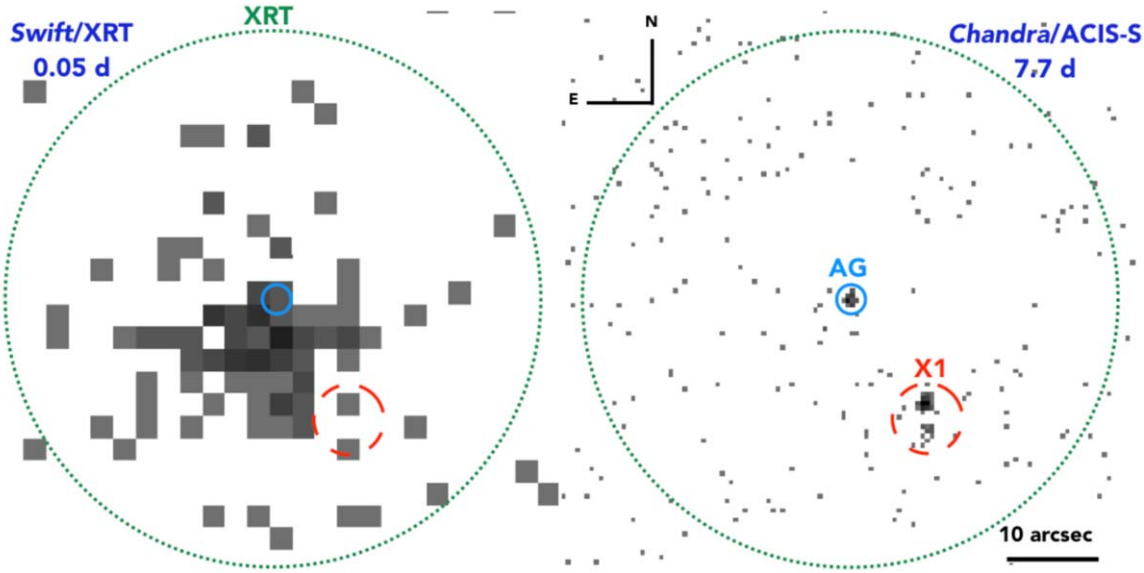

Figure 2. X-ray imaging of the Swift/XRT (left) and Chandra/ACIS-S (right) images of GRB 180418A in the 0.5–8 keV energy bands. The large dotted green circle indicates the XRT source subtraction region, while the blue circle shows the 3σ source region from the Chandra observation. The small dashed red region in both images shows X1, which adds an extra contribution to the count rate extracted from the XRT source region.

3.1.2. Swift/XRT Analysis

Given that X1 contaminates the afterglow position, we revise the Swift/XRT data of GRB 180418A to account for the contribution of flux from X1. We note that the automatic analysis of GRB 180418A[23] exhibits a flattening at $\delta t > 10^5$ s, most likely an indication of contamination from X1. The XRT observations span $\delta t = 3.88 \times 10^3$–$1.84 \times 10^6$ s, after which the flux fades below the XRT sensitivity limit (Figure 3; Evans et al. 2007, 2009). In total, nine XRT observations of the burst were obtained in PC mode (see Table 1).

We downloaded all of the XRT observations from the HEASARC archive. For the reduction of the XRT data, we used the HEASoft software (v.6.17; Blackburn et al. 1999; NASA High Energy Astrophysics Science Archive Research Center (HEASARC) 2014) and caldb files (v. 20170831). We produced new event files centered on the Chandra afterglow position utilizing the xrtpipeline tool and used them to perform the spectral analysis.

3.1.3. Joint X-Ray Spectral Analysis

First, we determine the count rates of the afterglow of GRB 180418A and X1 in the Chandra observations. We then obtain the spectral parameters of both sources and use them to revise the XRT light curve. To obtain the Chandra count rates, we use a circular region with a radius of 1.″5 centered on the Chandra afterglow position and obtain the background from a source-free annulus with inner and outer radii of 18.″5 and 34″, respectively. Using CIAO/dmextract, we obtain the afterglow net count rate of $(1.26 \pm 0.24) \times 10^{-3}$ counts s^{-1} and $(2.0 \pm 1.0) \times 10^{-4}$ counts s^{-1} from the first and third Chandra observations, respectively (see Table 1). For X1, we used a circular region with a radius of 3.″5, adjusted to encompass the entire complex (Figure 2), and a background annulus of the same size as that used for the afterglow. We generate the source and background spectra for both the afterglow and X1, as well as the necessary ancillary response file (arf) and redistribution matrix file (rmf) utilizing the CIAO specextract tool.

We first determine the spectral parameters of the Chandra observation at $\delta t \approx 7.7$ days, by fitting a model using Xspec (v.12.9.0; Arnaud 1996) for the spectrum within the 0.5–8 keV energy band. We choose a bin size to ensure at least one count per bin using the grppha task and to avoid any bin with negative net values when subtracting the background. In addition, we set the abundances to WILM (Wilms et al. 2000), the X-ray cross sections to VERN (Verner et al. 1996), and the statistics to W-statistics (statistics for background-subtracted Poisson data; Wachter et al. 1979). We employ a power-law model (pow) with two absorption components (tbabs), i.e., tbabs x tbabs x pow in Xspec, which represent the Galactic column density ($N_{\rm H,MW}$) and the intrinsic absorption value ($N_{\rm H,int}$). We fix the Galactic contribution to $N_{\rm H,MW} = 9.76 \times 10^{19}$ cm^{-2} (HI4PI Collaboration et al. 2016), while leaving the rest of the spectral parameters (including $N_{\rm H,int}$) free. The best-fit Chandra spectrum is characterized by a spectral photon index, $\Gamma_{\rm X} = 2.66^{+1.00}_{-0.73}$, and $N_{\rm H,int} < 5.4 \times 10^{21}$ cm^{-2} (1σ confidence). To obtain the unabsorbed flux ($F_{\rm X}$), we fix the spectral parameters to the best-fit values and use the convolution model, cflux, setting the energy range to 0.3−10 keV (Table 1). We repeat this procedure for the Chandra observation at $\delta t \approx 38.5$ days. The results of our spectral fits are listed in Table 1, and the unabsorbed fluxes are displayed in Figure 3.

We model the spectrum of X1 in the same manner as described above in all three Chandra observations, but instead employ a single-absorbed power-law model (tbabs x pow) in Xspec, as the consideration of the individual $N_{\rm H}$ contributions is not important here. We find that the spectral parameters of X1 at each epoch are consistent within 1σ errors and thus do not exhibit any significant evidence for spectral evolution between the three observations. Therefore, we link the spectral parameters between the three spectra of X1 and fit them simultaneously to better constrain the spectral shape of X1. We find that the best-fit power-law spectrum of X1 is characterized

[23] https://www.swift.ac.uk/xrt_curves/00826428/

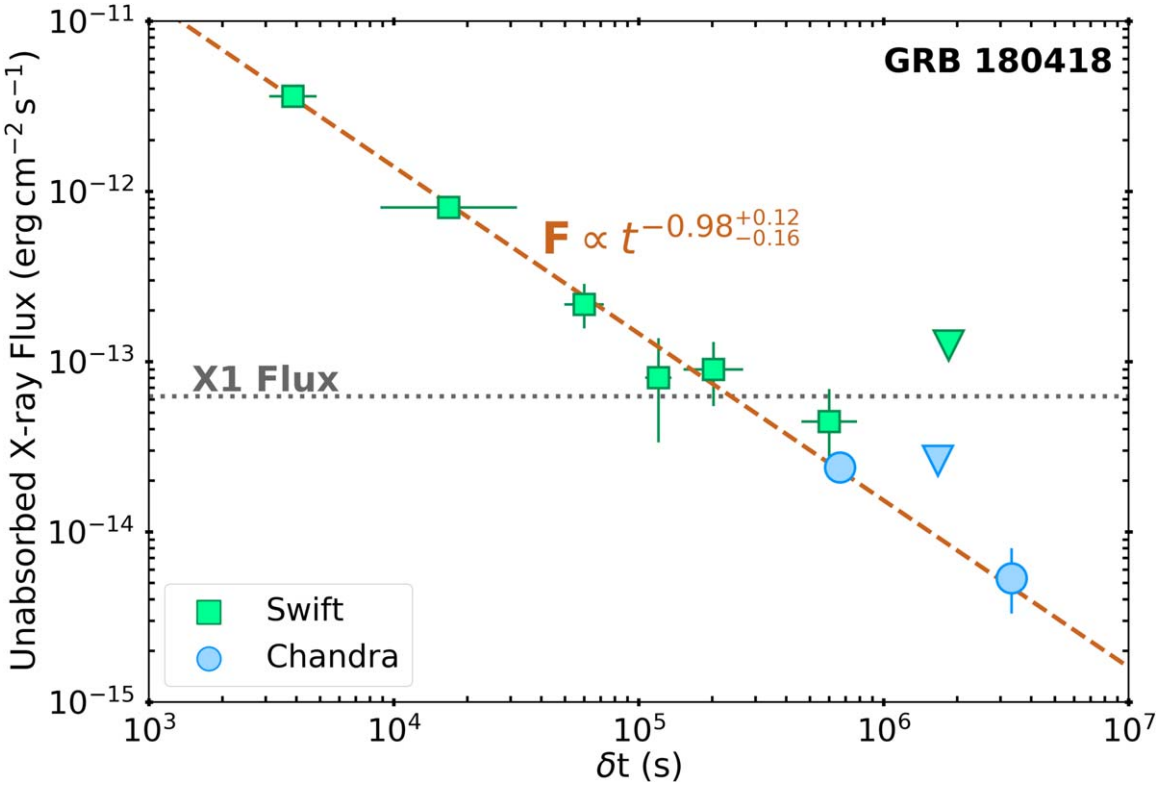

Figure 3. Swift/XRT (green squares) and Chandra/ACIS-S (blue circles) unabsorbed X-ray flux light curve (0.3–10 keV) for GRB 180418A. Each observation is log-centered, with the time errors denoting the duration of each observation. The flux errors are 1σ. In some cases, the symbols are bigger than the errors. The Swift and Chandra 3σ upper limits are indicated with green and blue arrows, respectively. The dashed light-brown line represents the best-fit single power-law model with $\alpha_X = -0.98^{+0.12}_{-0.16}$. The dotted horizontal gray line shows the unabsorbed X-ray flux level of X1, $\sim 6.24 \times 10^{-14}$ erg cm^{-2} s^{-1} (see Table 1).

by $\Gamma_{\rm X,X1} = 1.94^{+0.23}_{-0.17}$ and $N_{\rm H,X1} < 1.8 \times 10^{21}$ cm^{-2} (1σ confidence intervals).

To perform the spectral analysis of all nine Swift/XRT observations, we first combine the last four XRT observations in two groups (ObsIDs 0082642800[4-5] and 0082642800[6-7]) to ensure better statistics, resulting in seven epochs. We then obtain the spectrum of the afterglow for each observation utilizing the `Xselect` tool. For that, we use a circular source extraction region with a radius of $\sim$28.″28 centered at the afterglow position and a background annulus with inner and outer radii of $\sim$41.″44 and $\sim$259.″30, respectively, centered at the Chandra afterglow position. We use `grppha` again for binning our spectra in order to obtain a minimum of one count per bin. For each observation, we create the exposure maps with `xrtpipeline`, create the `arf` files with the `xrtmkarf` tool, and use the `rmf` files (v.14) for the spectral fitting.

We employ a two-component model to account for the combined presence of the afterglow and X1, using double- and single-absorbed power-law models, respectively. We use the `constant` multiplicative model to account for the cross-calibration between Swift/XRT-PC and Chandra/ACIS-S3. We set the XRT-PC constant value to 1 and calculate the ACIS-S3 constant value ($\texttt{const}_{\rm ACIS-S3} = 1.147$) using Table 5 from Plucinsky et al. (2017). To specifically obtain the unabsorbed fluxes from the afterglow in the 0.3–10 keV energy band, we set `cflux` only for the spectral component of the model that accounts for the afterglow as follows: `(tbabs x tbabs x const x cflux x pow)`$_{\rm AG}$ + `(tbabs x const x pow)`$_{\rm X1}$ in `Xspec`. The best-fit spectral parameters and unabsorbed fluxes with 1σ uncertainties are listed in Table 1 and shown in Figure 3. We only find significant adjustments to the XRT fluxes relative to the automatic pipeline values for the last three epochs, as the afterglow flux approaches the level of X1.

Finally, to derive upper limits from the XRT and Chandra observations where the afterglow is not detected, we extract the photons from the corresponding circular source regions centered on the afterglow Chandra position using `Xselect` and `CIAO/dmextract` tools, respectively. For the Swift observation at $\delta t \approx 21$ days, only three source photons are detected in $\sim$4.4 ks, while the same number of photons is obtained in $\sim$9.8 ks of Chandra observations at $\delta t \approx 19$ days. We use Poissonian confidence levels for small numbers of X-ray events according to Gehrels (1986) to calculate the 3σ count-rate upper limits and estimate the 3σ X-ray flux upper limits with the WebPIMMS tool[24] utilizing the best-fit spectral parameters of the first Chandra detection. These values are listed in Table 1.

3.2. Optical and Near-infrared Observations

In addition to the Swift/UVOT detection of the optical afterglow of GRB 180418A, there were several ground-based monitoring campaigns with optical facilities, including 25 cm Télescope à Action Rapide pour les Objets Transitoires (TAROT), RATIR mounted on the 1.5 m Harold L. Johnson Telescope (Becerra et al. 2019), 0.76 m Katzman Automatic Imaging Telescope (GCN 22647; Zheng & Filippenko 2018), 2 m Faulkes Telescope North (GCN 22648; Guidorzi et al. 2018), 1.5 m telescope at Observatorio de Sierra Nevada (GCN

[24] https://heasarc.gsfc.nasa.gov/cgi-bin/Tools/w3pimms/w3pimms.pl

Table 1
X-Ray Observations of GRB 180418A

ObsID	δt (s)	Exposure Time (s)	Γ_X	F_X (erg cm^{-2} s^{-1})
Swift/XRT				
0082642800 [0]	3.88×10^3	1.73×10^3	$2.02^{+0.29}_{-0.16}$	$3.62(^{+0.33}_{-0.31}) \times 10^{-12}$
+[1]	1.68×10^4	4.95×10^3	$1.70^{+0.22}_{-0.21}$	$8.04(^{+1.03}_{-0.96}) \times 10^{-13}$
+[2]	1.21×10^5	5.10×10^3	$1.3^{+3.2}_{-1.7}$	$8.1(^{+5.7}_{-4.7}) \times 10^{-14}$
+[3]	5.99×10^4	4.69×10^3	$1.50^{+0.61}_{-0.60}$	$2.17(^{+0.69}_{-0.60}) \times 10^{-13}$
+[4-5]	2.02×10^5	9.09×10^3	$1.39^{+1.11}_{-0.85}$	$9.0(^{+4.0}_{-3.5}) \times 10^{-14}$
+[6-7]	6.00×10^5	1.09×10^4	$2.5^{+6.7}_{-1.1}$	$4.4(^{+2.5}_{-2.1}) \times 10^{-14}$
+[8]	1.84×10^6	4.42×10^3	"	$< 1.2 \times 10^{-13}$
Afterglow, Chandra/ACIS-S				
20180	6.63×10^5	2.41×10^4	$2.66^{+1.00}_{-0.73}$	$2.40(^{+0.48}_{-0.43}) \times 10^{-14}$
20181	1.67×10^6	9.80×10^3	"	$< 2.6 \times 10^{-14}$
21092	3.33×10^6	2.76×10^4	"	$5.3(^{+2.7}_{-2.0}) \times 10^{-15}$
X1, Chandra/ACIS-S				
2018[0–1] and 21092	...	...	$1.94^{+0.23}_{-0.17}$	$6.24(^{+0.42}_{-0.40}) \times 10^{-14}$

Note. The elapsed time between the trigger of the burst and the observation is given by δt. The effective exposure times (after the data were filtered for background flares) are displayed in this table. The Galactic absorption column density ($N_{H,MW}$) was fixed to 9.76×10^{19} cm^{-2} (HI4PI Collaboration et al. 2016) during the spectral fitting process. Spectral photon indices (Γ_X) were obtained in the 0.5–8 keV energy range, while the unabsorbed X-ray fluxes (F_X) were calculated for the 0.3–10 keV band. Confidence intervals are 1σ. The 3σ flux upper limits were determined following the method described in Section 3.1.3

22657; Sota et al. 2018), 2.5 m Nordic Optical Telescope (GCN 22660; Malesani et al. 2018), 2.2 m MPG telescope (GCN 22662 and 22666; Schady 2018; Schady & Chen 2018), Xinglong 0.8 m Tsinghua-NAOC telescope (GCN 22661; Xin et al. 2018), 3.6 m Devasthal Optical Telescope (GCN 22663; Misra et al. 2018), 2.1 m Otto Struve telescope (GCN 22668; Choi et al. 2018), and Murikabushi 1 m telescope (GCN 22670; Horiuchi et al. 2018). In the following section, we report on our optical afterglow and host galaxy imaging.

3.2.1. Afterglow Imaging

We triggered target-of-opportunity (ToO) observations of the location of GRB 180418A with the Gemini Multi-Object Spectrograph (GMOS; Program GN-2018A-Q-121) mounted on the 8 m Gemini-North telescope on 2018 April 18 UT starting at $\delta t = 3.1$ hr. We obtained observations in the *griz* bands and used standard tasks in the IRAF/`gemini` package to create bias- and flat-field frames, apply them to the science images, and co-add the images in each filter. On the outskirts of the enhanced XRT position, we clearly detect an optical point source coincident with the Chandra X-ray position in all bands (Figure 4). The details of our observations are listed in Table 2.

To track the fading and color evolution of the source, we obtained an additional set of *griz*-band observations with the GMOS instruments mounted on the 8 m Gemini-North and Gemini-South telescopes on 2018 April 19 UT starting at $\delta t = 24.0$ hr, as well as *r*-band observations at two additional epochs of $\delta t = 2.89$ and 4.79 days. The last of these observations still clearly exhibits a detected source (Figure 4), necessitating late-time, deeper observations to assess the contribution from the underlying host galaxy (see Section 3.2.3). Therefore, we obtained *riz*-band observations of the field with Gemini-North/GMOS at $\delta t \approx 289$ days (Program GN-2018B-Q-117), which have significantly greater depth than the previous epochs and thus serve as adequate template images for the previous imaging. For each filter, we perform image subtraction between each of the earlier epochs and the late-time observation with the `HOTPANTS` software package (Becker 2015).

Calibrated to Sloan Digital Sky Survey (SDSS) DR12, we use `SExtractor` to derive an optical afterglow position of R.A. $= 11^h20^m29^s.20$ and decl. $= +24°55'58''.83$ (J2000) with a 1σ positional uncertainty of $0''.12$, including the contributions from the afterglow centroid and the astrometric tie uncertainty to SDSS. This position is fully consistent with the Chandra afterglow position (Figure 4). We perform aperture photometry on the residual images with the IRAF/`phot` package, using an aperture of $2.5 \times \theta_{FWHM}$ for each epoch and filter. The *r*-band afterglow observations are displayed in Figure 4, and the resulting photometry is listed in Table 2. We note that the data at $\delta t \approx 4.79$ days are based on differential photometry, and we do not include this point in subsequent fitting.

To place limits on any transient emission on timescales of $\gtrsim$few days, we also obtained near-infrared (NIR) imaging in the *J* and *K* bands with the Wide-field Camera (WFCAM; Casali et al. 2007) on the 3.8 m United Kingdom Infrared Telescope (UKIRT) at $\delta t \approx 6.0$ days. We obtained pre-processed images from the WFCAM Science Archive (Hamly et al. 2008), which are corrected for bias, flat-field, and dark current by the Cambridge Astronomical Survey Unit.[25] For each epoch and filter, we co-add the images and perform astrometry relative to the Two Micron All Sky Survey (2MASS) using a combination of tasks in Starlink[26] and IRAF. We do not detect any emission coincident with the afterglow, and we measure upper limits of $J \gtrsim 21.0$ mag and $K \gtrsim 21.1$ mag (calibrated to 2MASS and converted to the AB system) based on faint sources in the vicinity of the GRB position.

Finally, we obtained *J*-band observations with the Magellan Infrared Spectrograph (MMIRS) and *r*-band observations with Binospec, both mounted on the 6.5 m MMT (Multiple Mirror Telescope) at $\delta t \approx 10.9$ and 50.5 days, respectively. We used custom pipelines[27] using routines from `ccdproc` (Craig et al. 2017) and `astropy` (Astropy Collaboration et al. 2013; Price-Whelan et al. 2018) to perform bias subtraction, flat-fielding, and gain correction calibrations, as well as additional sky subtraction routines for MMIRS to take into account the varying IR sky. We aligned and co-added the data and calibrated to 2MASS and SDSS, respectively. Performing image subtraction with `HOTPANTS` relative to later template images (see Section 3.2.3), we place limits on late-time transient emission of $r \gtrsim 25.2$ mag (Table 2).

We briefly compare our limits to the luminosities of GRB-SNe. In particular, we compare the final *r*-band upper limit at $\delta t \approx 50$ days to the optical emission of GRB-SN 1998bw,

[25] http://casu.ast.cam.ac.uk/
[26] http://starlink.eao.hawaii.edu/starlink
[27] https://github.com/CIERA-Transients/Imaging_pipelines/blob/master/MMIRS_pipeline.py, https://github.com/CIERA-Transients/Imaging_pipelines/blob/master/BINOSPEC_pipeline.py

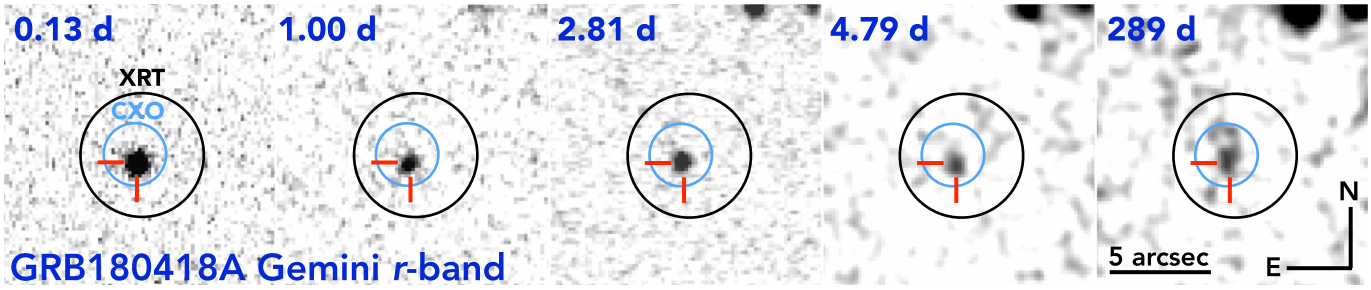

Figure 4. Gemini-North and Gemini-South GMOS r-band imaging sequence of the optical afterglow of GRB 180418A, over $\delta t = 0.13$–4.79 days. A deep, template image at $\delta t \approx 289$ days (last panel) reveals a faint, underlying host galaxy with $r = 25.69 \pm 0.21$ mag. The position of the optical afterglow (red cross-hairs) is coincident with the Chandra (CXO) position (3σ radius including astrometric uncertainty; blue circle) and the enhanced XRT position (3σ radius; black circle). The scale and orientation of the images are denoted in the last panel, and the last two panels have been smoothed for display purposes.

associated with the long GRB 980425 (Galama et al. 1998). At an assumed $z = 1$ (see Section 3.2.3), we find that our upper limit of $\nu L_\nu \gtrsim 7.8 \times 10^{42}$ erg s^{-1} is not deep enough to constrain the presence of an SN as luminous as SN 1998bw ($\approx 10^{42}$ erg s^{-1}; Clocchiatti et al. 2011) in the appropriate rest-frame band and time (U band and $\delta t_{rest} \approx 25.2$ days at $z = 1$). Only if GRB 180418A originated at lower redshifts of $z < 0.5$ could we effectively use this limit to rule out the existence of SN 1998bw-like emission.

3.2.2. Afterglow Spectroscopy

Using the Gemini-North rapid ToO program, we obtained a set of 4×900 s of spectroscopy of the optical afterglow (initially reported in Fong et al. 2018) on 2018 April 18 UT at a mid-time of $\delta t = 2.4$ hr. We obtained a pair of exposures with the R400 grating at each of two central wavelengths, 5200 and 5250 Å, covering a wavelength range of 4500–7600 Å. We used the Gemini IRAF package to apply bias and flat-field corrections, to apply cosmic-ray rejection, and to align and stack the frames. We additionally used CuAr lamp spectra for wavelength calibration that were taken during the observations, as well as a spectrum of standard star HZ44 taken on 2018 February 28 with the same setup to obtain a relative flux calibration. The resulting spectrum exhibits a featureless blue continuum, with no notable features in emission or absorption that could be attributed to the host galaxy. We note that the faintness of the host galaxy (Section 3.2.3) precludes a strong statement on the presence of emission features but overall exhibits no strong nebular emission.

3.2.3. Host Galaxy Observations

In Gemini imaging at $\delta t \approx 289$ days, we identify a faint galaxy at R.A. $= 11^{\rm h}20^{\rm m}29\overset{\rm s}{.}21$ and decl. $= +24°55'58\overset{''}{.}73$ (J2000), coincident with the Chandra and Gemini afterglow positions (Figure 4). We perform aperture photometry using the IRAF/`phot` package as previously described and measure a brightness of $r = 25.69 \pm 0.21$ mag. The galaxy is at an angular offset from the optical afterglow position of $0\overset{''}{.}16 \pm 0\overset{''}{.}04$. Using this offset and the r-band magnitude (Table 2), we calculate the probability of chance coincidence following the methods of Bloom et al. (2002a) to be $P_{cc} = 1.4 \times 10^{-3}$. The low value of P_{cc}, coupled with the fact that there are no other detectable $> 3\sigma$ sources within $7\overset{''}{.}5$ of the afterglow position to $r \gtrsim 26$ mag, solidifies this source as the host galaxy. The host galaxy is detected in riz bands, and the photometry results are in Table 2. We also obtain a deep upper limit with MMT/Binospec observations in g band of $g \gtrsim 25.7$ mag.

We additionally obtained NIR imaging observations in the $YJHK$ bands with the MMT/MMIRS. Only the J-band image yields a host galaxy detection of $J = 23.34 \pm 0.40$ mag. For the remaining filters, we calculate 3σ upper limits based on faint sources in the vicinity of the GRB in each image. The measurements and 3σ upper limits for the remaining filters are listed in Table 2.

4. Analysis and Results

4.1. Redshift Estimate

To estimate the redshift of GRB 180418A, we consider both the detection of the afterglow and the inferred luminosity of the host galaxy. The detection of the afterglow in the $uvm2$ UVOT filter (Siegel & D'Elia 2018), with $\lambda_{\rm max} \approx 2964$ Å (the wavelength at the upper end of the bandpass), automatically places an upper limit on the redshift of $z < 2.25$, corresponding to the Lyman limit of $\lambda = 912$Å at these redshifts, as a higher redshift would result in the complete suppression of flux at these wavelengths. On the other hand, the featureless afterglow spectrum implies that $z \gtrsim 1$ (or that the burst sight line did not intersect with any strong absorption features). Moreover, if GRB 180418A originated at the median redshift of short GRBs of $z = 0.5$, the inferred host luminosity would be low, with $L \lesssim 0.01 L^*$, where we expect only $\approx 5\%$ of the stellar mass at $z = 0.5$ to reside in galaxies fainter than this, implying that this is unlikely (Tomczak et al. 2014). Thus, we constrain a most likely redshift range of $z \approx 1$–2.25 for GRB 180418A. This is also in agreement with the results of Becerra et al. (2019), who found $z \approx 0.3 - 1.31$ based on the photometric upper limits and the combined X-ray, UV, and optical broadband spectral energy distribution.

4.2. Afterglow of GRB 180418A

4.2.1. Light-curve Fitting and Spectral Parameter Determination

To quantify the temporal evolution of the afterglow of GRB 180418A and the spectral information in the X-ray and optical bands, we consider the general relation $F_\nu \propto t^\alpha \nu^\beta$, where α and β are the temporal and spectral power-law indices, respectively. In particular, we determine $\alpha_{\rm X}$ and $\alpha_{\rm opt}$ by fitting the light curves in each band with a single power-law model, $F_\nu \propto t^\alpha$, using a χ^2-minimization procedure with a best-fit

Table 2
Afterglow and Host Galaxy Photometry of GRB 180418A

Date (UT)	δt (d)	Telescope	Filter	Exp. Time (s)	Afterglow (AB mag)	Host Galaxy (AB mag)	A_λ (AB mag)
2018 Apr 18.410	0.13	Gemini-N/GMOS	r	2×120	21.29 ± 0.06	⋯	0.039
2018 Apr 18.452	0.17	Gemini-N/GMOS	i	4×120	21.33 ± 0.16	⋯	0.029
2018 Apr 18.461	0.18	Gemini-N/GMOS	g	4×120	22.07 ± 0.15	⋯	0.056
2018 Apr 18.469	0.19	Gemini-N/GMOS	z	4×120	21.55 ± 0.10	⋯	0.022
2018 Apr 19.279	1.00	Gemini-N/GMOS	r	15×120	23.86 ± 0.13	⋯	0.039
2018 Apr 19.398	1.12	Gemini-N/GMOS	i	12×120	23.85 ± 0.08	⋯	0.029
2018 Apr 19.421	1.14	Gemini-N/GMOS	z	12×120	23.37 ± 0.29	⋯	0.022
2018 Apr 19.458	1.18	Gemini-N/GMOS	g	12×120	24.50 ± 0.31	⋯	0.056
2018 Apr 21.091	2.81	Gemini-S/GMOS	r	18×120	24.95 ± 0.13	⋯	0.039
2018 Apr 23.073	4.79	Gemini-S/GMOS	r	15×180	≈ 25.2[a]	⋯	0.039
2018 Apr 24.255	5.97	UKIRT/WFCAM	J	63×40	$\gtrsim 21.0$	⋯	0.012
2018 Apr 24.296	6.02	UKIRT/WFCAM	K	63×40	$\gtrsim 21.1$	⋯	0.005
2018 Apr 29.161	10.88	MMT/MMIRS	J	29×61.96	⋯	23.34 ± 0.40	0.012
2018 Jun 7.757	50.48	MMT/Binospec	r	13×180	$\gtrsim 25.2$	25.50 ± 0.43	0.039
2018 Nov 19	215	MMT/MMIRS	K	62×30.98	⋯	>22.0	0.005
2018 Nov 27	223	MMT/MMIRS	K	52×30.98	⋯	>22.4	0.005
2019 Feb 1	289[b]	Gemini-N/GMOS	r	14×120	⋯	25.69 ± 0.21	0.039
2019 Feb 1	289[b]	Gemini-N/GMOS	i	16×120	⋯	24.82 ± 0.14	0.029
2019 Feb 1	289[b]	Gemini-N/GMOS	z	20×90	⋯	24.62 ± 0.21	0.022
2019 Jun 18	426	MMT/MMIRS	H	91×30.98	⋯	$\gtrsim 22.8$	0.008
2020 Jan 10	632[b]	MMT/MMIRS	J	29×61.96	⋯	$\gtrsim 23.3$	0.012
2020 Mar 5	687	MMT/MMIRS	Y	30×119.49	⋯	$\gtrsim 23.3$	0.012
2020 Nov 20	947	MMT/Binospec	g	20×60	⋯	$\gtrsim 25.7$	0.056

Notes.
[a] While the HOTPANTS residual image for this epoch does not exhibit any source of meaningful significance, there is clearly afterglow flux contributing at this epoch based on differential photometry. The value reported here is thus based on differential photometry, assuming $r = 25.69$ AB mag for the host galaxy. We do not, however, include this data point in our fitting.
[b] These observations serve as template images to compute earlier afterglow fluxes. Limits correspond to 3σ confidence, and uncertainties correspond to 1σ. Magnitudes are corrected for Galactic extinction (Schlafly & Finkbeiner 2011).

normalization defined by

$$\mathrm{C} = \frac{\sum_{i=1}^{N} \frac{F_{\mathrm{model,i}} \times F_{\nu,i}}{\sigma_{\nu,i}^2}}{\sum_{i=1}^{N} \frac{F_{\mathrm{model,i}}^2}{\sigma_{\nu,i}^2}}, \quad (1)$$

where $F_{\mathrm{model,i}}$ and $F_{\nu,i}$ are the unnormalized and observed fluxes, respectively, $\sigma_{\nu,i}$ are the uncertainties on the fluxes, and N is the number of data points.

To fit the X-ray light curve, we include all data points (see Figure 3). For the optical afterglow, since we are only interested in the forward shock (FS) afterglow behavior, we ignore data at $\delta t \leqslant 100$ s in the r-band light curve, as there is an initial flux density enhancement that has been attributed to a reverse shock (RS; Figure 5; Becerra et al. 2019; and Section 4.3), and include all available data in the giz bands. The final temporal indices we obtain are $\alpha_{\mathrm{X}} = -0.98^{+0.12}_{-0.16}$ and $\langle \alpha_{\mathrm{opt}} \rangle = -1.01 \pm 0.03$ with 1σ uncertainties, where $\langle \alpha_{\mathrm{opt}} \rangle$ is the weighted mean of the temporal indices corresponding to the four optical bands: $\alpha_{\mathrm{g}} = -0.97 \pm 0.13$, $\alpha_{\mathrm{r}} = -1.01^{+0.03}_{-0.04}$, $\alpha_i = -1.03 \pm 0.04$, and $\alpha_{\mathrm{z}} = -0.93^{+0.14}_{-0.16}$.

We determine the X-ray spectral index, β_{X}, from the relation $\beta_{\mathrm{X}} \equiv 1 - \Gamma_{\mathrm{X}}$, where Γ_{X} is the X-ray spectral photon index. We calculate the value of β_{X} for each X-ray observation using the Γ_{X} spectral values and obtain the weighted mean of $\langle \beta_{\mathrm{X}} \rangle = -0.85 \pm 0.14$ (1σ uncertainty). In the case of the optical band, we utilize contemporaneous observations at $\delta t \approx 0.13$–0.19 days in the Gemini $griz$ bands and extrapolate them to a common time of $\delta t \approx 0.13$ days to determine β_{opt}. We use χ^2-minimization to fit a single power law, finding $\beta_{\mathrm{opt}} = -0.70 \pm 0.19$ (1σ uncertainty).

4.2.2. Energy and Circumburst Density Properties

In this section, we model the detected emission from GRB 180418A in the different bands (optical and X-rays) and limits (NIR and radio) in the framework of the standard synchrotron FS model. In this scenario, the broadband emission originates from an FS resulting from the interaction of the relativistic GRB jet with the surrounding environment (Sari et al. 1998; Granot & Sari 2002). The model is defined by the following parameters: isotropic-equivalent energy of the jet ($E_{\mathrm{K,iso}}$), circumburst density (n), power-law index of accelerated electrons (p), fractions of the post-shock energy transmitted to electrons (ϵ_{e}) and magnetic field (ϵ_{B}), and the opening angle of the jet (θ_j). Likewise, the synchrotron spectral shape is characterized by the synchrotron self-absorption frequency (ν_{sa}), the synchrotron peak frequency (ν_m), and the cooling frequency (ν_c).

First, we determine the position of the X-ray band with respect to the cooling frequency, assuming a constant-density medium. For that, we calculate the value of p using the relations between the temporal and spectral indices introduced by Granot & Sari (2002). We require the value of p to be consistent within the errors in one of the next two scenarios: $\nu_{\mathrm{X}} > \nu_{\mathrm{c}}$ or $\nu_{\mathrm{m}} < \nu_{\mathrm{X}} < \nu_{\mathrm{c}}$. For $\nu_{\mathrm{X}} > \nu_{\mathrm{c}}$, we find that the values of p are inconsistent and, furthermore, lead to $p < 2$. This is an

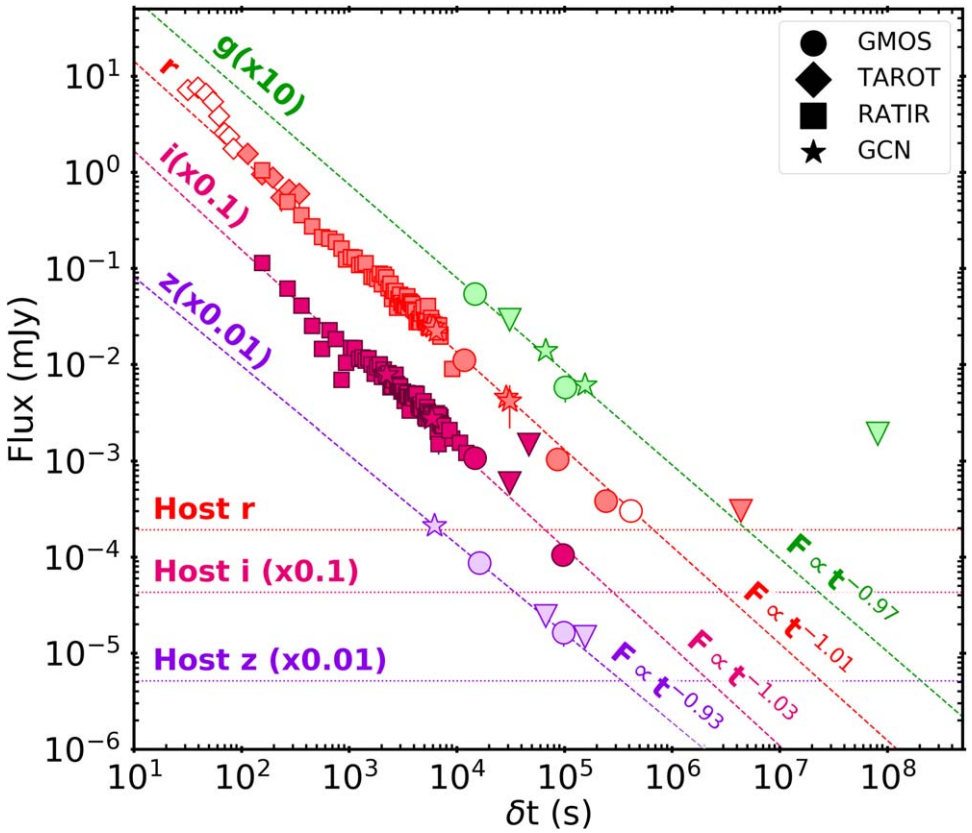

Figure 5. Optical afterglow light curves of GRB 180418A in the *griz* filters. Circles represent our new Gemini afterglow data (Table 2). Literature data from TAROT (diamonds), RATIR (squares), and other sources (stars) are also shown (Choi et al. 2018; Guidorzi et al. 2018; Horiuchi et al. 2018; Malesani et al. 2018; Misra et al. 2018; Schady 2018; Schady & Chen 2018; Sota et al. 2018; Xin et al. 2018; Becerra et al. 2019). Triangles indicate 3σ upper limits. Only those observations in the *riz* filters for which the host galaxy contribution is less than 5% of the total optical flux are plotted. Observations in the *r* band that are ignored in the power-law fit are shown as open symbols. Horizontal lines denote the flux of the host galaxy, while dashed lines indicate the best-fit power-law decay models for the different bands.

unlikely value since p generally ranges between 2 and 3 as a direct consequence of the Lorentz factor distribution (e.g., de Jager & Harding 1992). On the other hand, for $\nu_m < \nu_X < \nu_c$, we obtain consistent values of p within the errors for both X-ray and optical bands. Therefore, we accept the scenario where $\nu_m < \nu_{opt} < \nu_X < \nu_c$ for the duration of the observations, and we calculate a weighted mean value of $\langle p \rangle = 2.39 \pm 0.12$.

In addition, given the borderline nature of the classification of GRB 180418A (short vs. long), we briefly explore the possibility that the shock wave expands into a wind medium, with $n(r) \propto r^{-2}$, as expected for massive star progenitors. We follow the consequent closure relations for a wind environment from Granot & Sari (2002) but find inconsistent values of p, as well as $p < 2$ for both of the aforementioned scenarios. Given that a large fraction of bona fide long GRB afterglows are inconsistent with the wind medium solution (Racusin et al. 2009; Schulze et al. 2011; Laskar et al. 2018), we note that this alone is not conclusive as to the nature of the progenitor for GRB 180418A. For our subsequent analysis, we consider a constant-density interstellar medium (ISM).

Next, we constrain the physical burst properties, $E_{K,iso}$ and n, utilizing the data in the X-ray and optical bands, and the radio upper limit. Specifically, we use $F_{\nu,X} = (2.48 \pm 0.23) \times 10^{-4}$ mJy at $\delta t \approx 0.05$ days and $\nu_X = 4.19 \times 10^{17}$ Hz (log-centered frequency of the 0.3−10 keV energy band), $F_{\nu,opt} = (1.10 \pm 0.12) \times 10^{-2}$ mJy at $\delta t \approx 0.13$ days and $\nu_{opt} = 4.84 \times 10^{14}$ Hz, and $F_{\nu,radio} < 9.9 \times 10^{-2}$ mJy at $\delta t \approx 0.61$ days and $\nu_{radio} = 15.5 \times 10^{9}$ Hz. We calculate the $E_{K,iso}$–n relations set by the broadband observations, fixing the value of ϵ_e to 0.1 (Panaitescu & Kumar 2002; Sironi & Spitkovsky 2011) and varying the value of ϵ_B between 10^{-4} and 0.1 considering $z = 1$ and 1.5. Assuming $\nu_{sa} < \nu_{radio} < \nu_m$ and $\nu_m < \nu_{opt} < \nu_X < \nu_c$, we set the minimum value of the cooling frequency ($\nu_{c,min} = 2.4 \times 10^{18}$ Hz) equal to the upper edge of the X-ray band (equivalent to 10 keV), which translates to an upper limit on the $E_{K,iso}$–n parameter space. Finally, we set the minimum value of the circumburst density to $n_{0,min} = 10^{-4}$ cm^{-3}, determined by the low end of typical ISM particle densities.

Combining the probability distributions of $E_{K,iso}$ and n and assuming values of ϵ_B ranging between 0.1 and 10^{-4}, we find that $E_{K,iso} = (0.89 - 29) \times 10^{52}$ erg and $n = (2.56 - 56) \times 10^{-4}$ cm^{-3} at $z = 1$, whereas $E_{K,iso} = (1.64–35) \times 10^{52}$ erg and $n = (2.21 - 160) \times 10^{-4}$ cm^{-3} at $z = 1.5$. Lastly, we use these values of $E_{K,iso}$ and $E_{\gamma,iso}$ (Section 2.2) to calculate the γ-ray efficiency of $\eta \approx 0.2 - 0.01$ at $z = 1$ and $\eta \approx 0.1 - 0.01$ at $z = 1.5$. The results are listed in Table 3.

4.2.3. Constraints on the Jet Opening Angle

Here, we study our late-time monitoring of the X-ray afterglow to determine the jet opening angle (θ_j) of GRB 180418A. In the fireball model, the observed temporal behavior from a spherical expansion for an on-axis observer is initially similar to that of a collimated relativistic outflow (Meszaros & Rees 1992, 1993; Rees & Meszaros 1992;

Table 3
GRB 180418A Burst Properties and Circumburst Density

Case	ϵ_B	$E_{K,iso}$ (erg)	n_0 (cm^{-3})	$\langle\theta_{j,min}\rangle$ (deg)	f_b	$E_{K,lim}$ (erg)	$E_{\gamma,lim}$ (erg)	η
			$z = 1$					
Case A	0.1	$(8.9^{+1.1}_{-1.0}) \times 10^{51}$	$(2.56^{+0.88}_{-0.66}) \times 10^{-4}$	$10.45^{+0.52}_{-0.53}$	0.017	1.51×10^{50}	4.61×10^{49}	0.23
Case B	10^{-2}	$(2.07^{+1.22}_{-0.77}) \times 10^{52}$	$(1.7^{+4.2}_{-1.2}) \times 10^{-3}$	$11.9^{+2.9}_{-2.3}$	0.022	4.55×10^{50}	5.96×10^{49}	0.12
Case C	10^{-3}	$(4.8^{+6.0}_{-2.7}) \times 10^{52}$	$(1.1^{+9.1}_{-1.0}) \times 10^{-2}$	$13.6^{+6.2}_{-4.2}$	0.028	1.34×10^{51}	7.59×10^{49}	0.05
Case D	10^{-4}	$(2.9^{+1.9}_{-1.2}) \times 10^{53}$	$(5.6^{+16.2}_{-4.1}) \times 10^{-3}$	$9.9^{+2.6}_{-2.1}$	0.015	4.4×10^{51}	4.1×10^{49}	0.009
			$z = 1.5$					
Case E	0.1	$(1.64 \pm 0.10) \times 10^{52}$	$(2.21^{+0.17}_{-0.16}) \times 10^{-4}$	$8.74^{+0.13}_{-0.12}$	0.012	1.97×10^{50}	7.14×10^{49}	0.14
Case F	10^{-2}	$(3.8^{+1.8}_{-1.2}) \times 10^{52}$	$(1.47^{+2.61}_{-0.94}) \times 10^{-3}$	$9.9^{+1.9}_{-1.6}$	0.015	5.7×10^{50}	8.9×10^{49}	0.07
Case G	10^{-3}	$(8.9^{+9.6}_{-4.6}) \times 10^{52}$	$(9.8^{+60.5}_{-8.4}) \times 10^{-3}$	$11.4^{+4.5}_{-3.2}$	0.020	1.78×10^{51}	1.19×10^{50}	0.03
Case H	10^{-4}	$(3.5^{+3.7}_{-1.8}) \times 10^{53}$	$(1.6^{+9.2}_{-1.3}) \times 10^{-2}$	$10.1^{+4.0}_{-2.9}$	0.016	5.6×10^{51}	9.5×10^{49}	0.008

Note. The median values of the isotropic-kinetic energy ($E_{K,iso}$) and circumburst density (n_0) for values of $\epsilon_B = 0.1$ to 10^{-4} at $z = 1$ and 1.5 (cases A–D and cases E–H, respectively). The median values of the minimum opening angle of the jet (Section 4.2.3) for each case are represented by $\langle\theta_{j,min}\rangle$. The parameter f_b is the beaming factor, and $E_{K,lim}$ corresponds to the lower limit of the true γ-ray and kinetic energy values. The η parameter is defined as $E_{\gamma,iso}/(E_{K,iso}+E_{\gamma,iso})$. Errors are 1σ.

Sari & Piran 1995). As the value of the bulk Lorentz factor (Γ) declines over time to reach a value of θ_j^{-1} (Piran 1995), a significant temporal steepening in the afterglow light curve is expected for a collimated outflow, known as a "jet break" (Sari et al. 1999; van Eerten & MacFadyen 2013), after which the flow may undergo lateral expansion (Granot & Piran 2012). From the detection of the jet break in the afterglow light curve at a certain time, one can derive the GRB jet opening angle. In contrast, a spherical outflow is expected to decline as a single power law until it reaches the nonrelativistic regime (Taylor 1950; Sedov 1959; van Eerten et al. 2010; Sironi & Giannios 2013).

For GRB 180418A, the optical afterglow in the *griz* bands exhibits a single power-law decline to $\delta t \approx 2.8$ days. In the X-ray band, the afterglow light curve of GRB 180418A is well modeled as a single power-law decay up to $\delta t \approx 38.5$ days and does not show any noticeable deviation from this decline rate. Thus, we can determine a lower limit for θ_j by using the time of the last Chandra observation ($\delta t = 38.515$ days), following the relation given by Sari et al. (1999) and Frail et al. (2001),

$$\theta_j \geqslant 37.53(1+z)^{-3/8} E_{K,iso,52}^{-1/8} n_0^{1/8} \quad (\text{deg}), \tag{2}$$

where $E_{K,iso,52}$ is in units of 10^{52} ergs and n_0 is in units of cm^{-3}. We calculate the minimum value, $\theta_{j,min}$, using Equation (2) for every allowed pair of $E_{K,iso} - n$ as determined in Section 4.2.2, and we compute the resulting cumulative probability distribution for each value (Figure 9). The median values of the minimum opening angles, $\langle\theta_{j,min}\rangle$, are listed in Table 3. Given that we do not detect a jet break in the afterglow light curve, we determine lower limits of $\langle\theta_{j,min}\rangle = 9.^\circ9$–$13.^\circ6$ for $z = 1$ and $\langle\theta_{j,min}\rangle = 8.^\circ74$–$11.^\circ4$ for $z = 1.5$. This is in agreement with the result reported in Becerra et al. 2019, where the jet opening angle is constrained to $\theta_j \geqslant 7^\circ$ considering $z = 0.5$ and the multiwavelength information up to 0.8 days. We further note that if higher values for the density (≈ 0.1 cm^{-3}) and/or lower values of $\epsilon_B \lesssim 10^{-4}$ are considered, as suggested by the multiwavelength modeling, then we obtain a wider opening angle constraint of $\theta_{j,min} \approx 17^\circ$ for $z = 1$.

Finally, we calculate the beaming correction factor (defined as $f_b \equiv [1 - \cos(\theta_j)]$). For every value of $\langle\theta_{j,min}\rangle$, we obtain lower limits on the true kinetic energy, $E_K = f_b E_{K,iso}$, as a wider jet would indicate a value closer to the isotropic-equivalent value. For the different values of ϵ_B considered in this work, we obtain $E_{K,lim} = (1.51 - 44) \times 10^{50}$ erg at $z = 1$ and $E_{K,lim} = (1.97 - 56) \times 10^{50}$ erg at $z = 1.5$ (see Table 3).

4.3. Reverse Shock Scenario

Here, we explore the broadband emission of GRB 180418A in the context of a combined FS and RS model, the latter of which propagates back into the ejecta, decelerating it (Sari et al. 1998; Zhang & Kobayashi 2005). This is in part motivated by the results of Becerra et al. (2019), which explained the *r*-band afterglow at $\delta t \lesssim 10^{-3}$ days with an RS model (Figure 6). As the early optical and radio observations are the most relevant for this component, we first consider the locations of ν_{radio} and ν_{opt} with respect to ν_m at early times. At the time of the first radio upper limit, $\delta t \approx 0.61$ days, we calculate a limit on the radio to optical spectral index of $\beta_{radio-opt} \gtrsim -0.36$, which is shallow compared to $\beta_{opt} \approx -0.7$ (Section 4.2.1). This indicates that $\nu_{radio} < \nu_m < \nu_{opt}$ at this time; this constraint allows us to derive limits on the peak frequency and flux of the FS of $\nu_m \gtrsim 4.7 \times 10^{11}$ Hz and $F_{\nu,FS,max} \lesssim 0.3$ mJy, respectively.

In the constant-density environment considered here, and which is also favored by the shallow optical and X-ray decay at $\delta t \gtrsim 0.02$ days (Figure 6), the peak flux of the spectrum remains constant as ν_m cascades to lower frequencies owing to adiabatic cooling. However, the observed *r*-band flux remains greater than $F_{\nu,FS,max}$ at early times, peaking at ≈ 7 mJy, or at least a factor of ≈ 23 brighter (Figure 6). Furthermore, the limit on $\nu_{m,FS}$ implies that $\nu_{m,FS}$ passes through *r* band at $\delta t \gtrsim 5 \times 10^{-3}$ days. Thus, the *r*-band emission at early times is too bright to be explained solely by FS emission.

One possible mechanism that can produce radiation in excess of the FS emission in the optical bands at early times is an RS. Early excess optical emission has been ascribed to an RS component for many long-duration GRBs (Laskar et al. 2018, 2019), as well as for two short-duration GRBs, GRB 051221A and GRB 160821B (Soderberg et al. 2006; Lloyd-Ronning 2018; Lamb et al. 2019), and possibly GRB 200522A (Fong et al. 2021). Similar to that for the FS, the RS synchrotron spectrum is also characterized by an injection break ($\nu_{m,RS}$) and cooling break ($\nu_{c,RS}$), as well as a

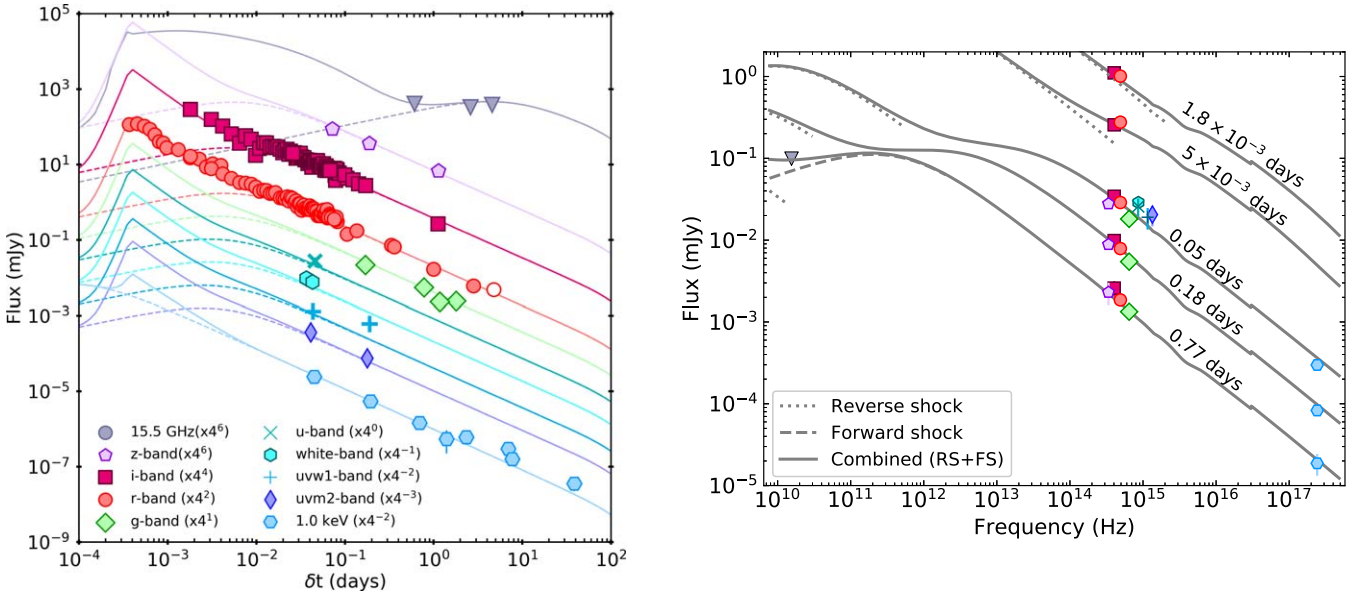

Figure 6. Left: radio to X-ray light curves of the GRB 180418A afterglow and the best-fit RS+FS model (solid lines) with a magnetization parameter of $R_B \approx 5.2$ and an initial jet Lorentz factor of $\Gamma_0 \approx 150$. For each band, the FS component is indicated with dashed lines. For completion, we have considered the UVOT data (converted to the AB system and corrected for Galactic extinction) reported by Siegel & D'Elia (2018) in our modeling. Open symbols indicate data that are not included in the fitting (see Section 3.2.1). Right: radio to X-ray spectral energy distribution of the GRB 180418A afterglow spanning from 1.8×10^{-3} days to 0.77 days after the burst, together with the best-fit model (solid lines) decomposed into RS (dotted) and FS (dashed) components. The radio upper limit constrains the peak flux and frequency of the FS spectrum, necessitating an RS component in the optical before ≈ 0.05 days.

self-absorption break ($\nu_{a,RS}$), although the latter cannot be constrained by our present data. RS emission is expected to peak at the deceleration time, t_{dec}, when the RS reaches the back of the jet. The subsequent light curves depend on the hydrodynamics of the reverse-shocked shell, which, for short-duration GRBs, are expected to follow the thin-shell regime ($t_{dec} \gtrsim T_{90}$), resulting in a Newtonian RS (Kobayashi 2000). In this regime, the post-shock bulk Lorentz factor evolves with radius as $\Gamma \propto R^{-g}$, where g is ≈ 2.2 in a uniform-density external environment (Kobayashi & Sari 2000). Considering $g \approx 2.2$ and $p \approx 2.4$ (as inferred for the FS) and the equations for $F_{m,RS}$ at $\nu < \nu_{m,RS}$ and $\nu > \nu_{m,RS}$ introduced by Kobayashi & Sari (2000) in their Section 3.3, we expect $\alpha \approx -0.46$ before the passage of $\nu_{m,RS}$ and $\alpha \approx -2.0$ thereafter. The observed α_r of -1.38 ± 0.03 lies between these expected limits at $(0.4 - 5) \times 10^{-3}$ days.

One explanation may be that for the observed r-band light curve at $\lesssim 5 \times 10^{-3}$ days $\nu_{m,RS}$ is in the r band around this time ($\approx 10^{-3}$ days). However, this produces an impossibly low initial bulk Lorentz factor (Γ_0) for the jet. Taking the most extreme scenario of $\nu_{m,FS}$ and $\nu_{m,RS}$ passing through r band at the latest and earliest possible times, $\approx 10^{-2}$ days and $\approx 4 \times 10^{-4}$ days, respectively (pushing them apart to the greatest degree), the initial bulk Lorentz factor[28] Γ_0 is $\lesssim 11$. At the same time, the FS Lorentz factor $\Gamma_{FS} \approx 150$ for $E_{K,iso} \approx 6 \times 10^{52}$ erg and $n_0 \approx 0.1$ cm^{-3} (following the closure relations in Section 4.2.2). A jet with $\Gamma_0 \approx 11$ cannot set up an FS with a Lorentz factor of $\Gamma \approx 150$. Hence, it is unlikely that the relatively shallow optical light curve at $\lesssim 5 \times 10^{-3}$ days is due to the passage of $\nu_{m,RS}$.

An alternate possibility is to relax the assumption of $g \approx 2.2$. Higher values of g have been inferred for long-duration GRBs in the past, with $g \approx 5$ for GRB 130427A (Laskar et al. 2013; Perley et al. 2014) and $g \approx 2.7$ for GRB 181201A (Laskar et al. 2019), each greater than the expected value of $g \approx 1$ for a wind-like environment (Zou et al. 2005). In our case of GRB 180418A, we find that $\alpha_r \approx -1.8$ for $g \approx 5$. While this is still too steep to completely explain the observed decline rate, the addition of the FS component ameliorates the remaining tension. For $z = 1.0$, we find that an RS+FS model gives consistent parameters that we derived for the FS alone; for p, the explosion properties and microphysical parameters. In addition, we find that $t_{dec} \approx 3.8 \times 10^{-4}$ days, $\nu_{m,RS}(t_{dec}) \approx 10^{13}$ Hz, and $\nu_{c,RS}(t_{dec}) \approx 6 \times 10^{18}$ Hz fit the multifrequency data self-consistently. In Figure 6 we present our best-fit light curves using the combined RS+FS model with parameters $p = 2.4$, $\epsilon_e = 0.13\zeta$, $\epsilon_B = 10^{-4}\zeta^{-3}$, $n_0 = 0.1\zeta^5$ cm^{-3}, and $E_{K,iso} = 6.2 \times 10^{52}\zeta^{-2}$ erg. The parameter $\zeta = \frac{1+z}{2}$ analytically encapsulates the additional degeneracy in these parameters owing to the unknown redshift. For this model, we find an RS magnetization of $R_B \equiv \sqrt{\epsilon_{B,RS}/\epsilon_{B,FS}} \approx 5.2$ and an initial jet Lorentz factor $\Gamma_0 \approx 150 \approx \Gamma_{FS}(t_{dec})$, which is commensurate with a nonrelativistic RS. Although the bulk Lorentz factor we obtain is similar to that reported by Becerra et al. (2019), $\Gamma_0 \approx 160$, our RS magnetization parameter and $E_{K,iso}$ are below and above, respectively, the reported values by these authors[29] ($R_B \approx 14$ and $E_{K,iso} \approx 0.77 \times 10^{51}$ erg).

5. X-Ray Afterglow Comparison

In the following section, we compare the X-ray afterglow behavior of GRB 180418A to the Swift short and long GRB populations, by performing a systematic comparison of their 0.3–10 keV Swift/XRT luminosities (L_X) and temporal behavior. We obtain the XRT flux light curves (Evans et al. 2007, 2009)

[28] Defined as $\Gamma_0 \approx (\nu_{m,FS}(t_{dec})/\nu_{m,RS}(t_{dec}))^{1/2}$, where $t_{dec} \approx 4 \times 10^{-4}$ days and $\nu_{m,FS} \propto t^{-3/2}$.

[29] We believe that there may be a typographical error in Becerra et al. (2019), where the reported value of $E_{K,iso}$ is incorrect by a factor of 10. Using their values of the other parameters, we infer that $E_{K,iso} \approx 6 \times 10^{51}$ erg would be required to match the X-ray and optical light curves.

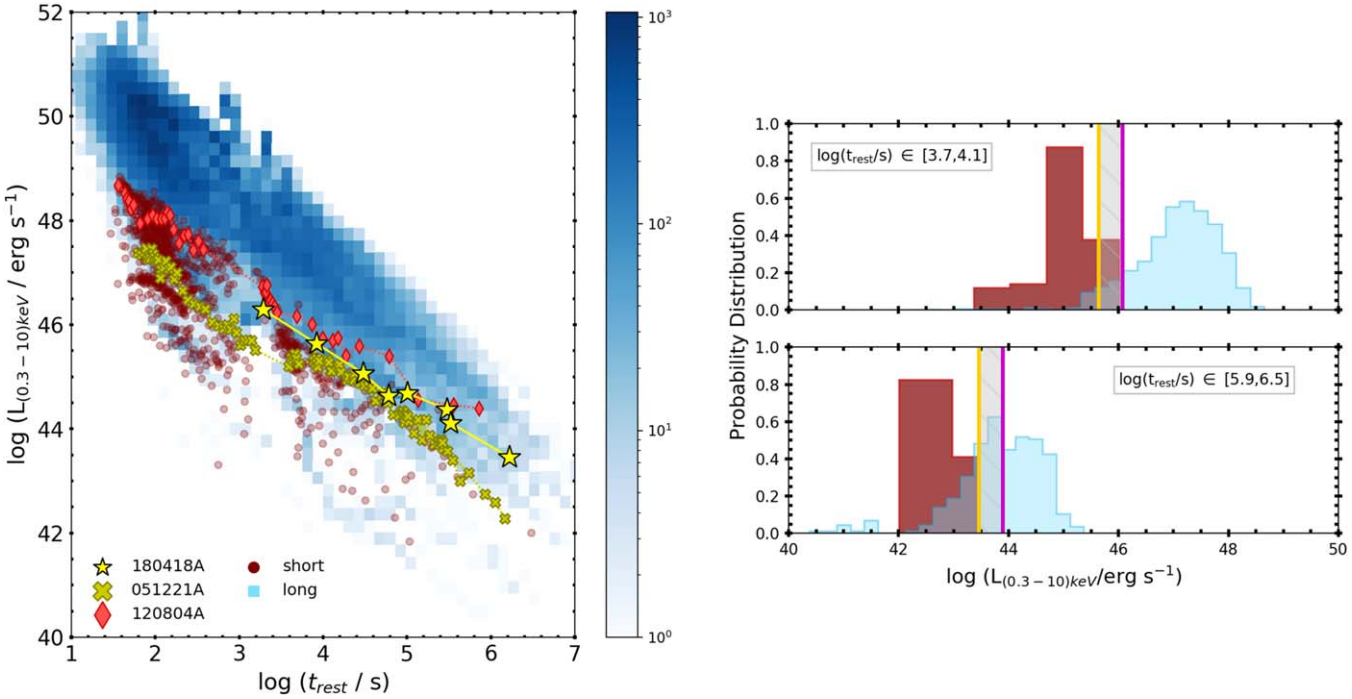

Figure 7. Left: X-ray luminosity (0.3–10.0 keV) vs. rest-frame time plot of all the GRBs detected by Swift/BAT with known redshifts. The long GRB population ($T_{90} > 2$ s) is shown in blue, where the different shades in color represent the density of available data. The short GRB population ($T_{90} \leqslant 2$ s) is represented by deep red circles. For plotting purposes, we only show the X-ray luminosity light curve of GRB 180418A at $z = 1$ (yellow stars). Those short GRBs that display similar X-ray behavior to GRB 180418A (Section 5) are shown with different symbols (yellow crosses and red diamonds). Right: distribution of the X-ray luminosity (0.3–10.0 keV) for the short (red) and long (blue) GRB populations at $\log(\delta t_{\rm rest}\ {\rm s}^{-1}) \approx 4$ (top panel) and $\log(\delta t_{\rm rest}\ {\rm s}^{-1}) \approx 6$ (bottom panel). The gray shaded area indicates the potential X-ray luminosity values for the GRB 180418A afterglow considering redshift values between $z = 1$ and 1.5. The X-ray luminosity of the afterglow at $z = 1$ is shown with dark-yellow vertical lines, while the dark pink vertical lines indicate the luminosity at $z = 1.5$.

for the GRBs with known redshifts, resulting in 37 short GRBs and 350 long GRBs. We also include the late-time ($\log(\delta t_{\rm rest}/{\rm s}) \gtrsim 5$) Chandra and XMM-Newton data in the light curves if available, i.e., for GRB 051221A (Burrows et al. 2006), GRB 120804A (Berger et al. 2013), and GRB 150101B (Fong et al. 2016). We calculate the $L_{\rm X}$ and rest-frame times ($t_{\rm rest}$) for each GRB and plot the light curves in the left panel of Figure 7. To compare the X-ray afterglow behavior of GRB 180418A with the short and long GRB populations, we calculate the characteristic median and 1σ dispersion values for both populations: $\log(L_{\rm X,short}/{\rm erg\ s^{-1}}) = 45.18^{+0.51}_{-0.21}$ and $\log(L_{\rm X,long}/{\rm erg\ s^{-1}}) = 47.14^{+0.84}_{-0.63}$ at $\log(\delta t_{\rm rest}\ {\rm s}^{-1}) \approx 4$, and $\log(L_{\rm X,short}/{\rm erg\ s^{-1}}) = 42.60^{+0.41}_{-0.42}$ and $\log(L_{\rm X,long}/{\rm erg\ s^{-1}}) = 43.90^{+0.70}_{-0.69}$ at $\log(\delta t_{\rm rest}\ {\rm s}^{-1}) \approx 6$.

Assuming a redshift of $z = 1$ for GRB 180418A, we find that the X-ray afterglow luminosity at earlier times ($\log(\delta t_{\rm rest}/{\rm s}) \approx 4$) of $\log(L_{\rm X}/{\rm erg\ s^{-1}}) \approx 45.6$ is subluminous compared to the majority of long GRBs, falling 2.5σ below the median $L_{\rm X}$ of this population at this time, but it is just above the short GRB median, and within the 1σ uncertainty (Figure 7). On the other hand, at late times ($\log(\delta t_{\rm rest}/{\rm s}) \approx 6$), we find that the X-ray luminosity of GRB 180418A, $\log(L_{\rm X}/{\rm erg\ s^{-1}}) \approx 43.5$, is within the 1σ uncertainty region of the long GRB population, almost 2σ above the median of the X-ray luminosity of short GRBs (Figure 7, right panel). However, for short GRBs, there exists very sparse information at these late epochs owing to their faintness, and in fact, the majority of all available information comes from Chandra and XMM-Newton observations. We find similar results assuming $z = 1.5$ (Figure 7, right).

It is useful to explore the properties of the subsets of long and short GRBs that exhibit similar X-ray light-curve behavior to GRB 180418A. To determine the subsets that track the X-ray afterglow behavior of GRB 180418A, we select those events with detections within a log-spaced interval of 5% of the GRB rest-frame δt and X-ray luminosity for $\log(\delta t_{\rm rest}/{\rm s}) \leqslant 5.6$. This interval was chosen to represent the temporal behavior probed by GRB 180418A, while also optimizing the number of GRBs in each sample that fit these criteria. Our criteria are satisfied for 2/37 short GRBs and 103/350 long GRBs. If we consider a fiducial value for the redshift of $z = 1.5$, our criteria are not satisfied for any short GRB.

The two short GRBs with similar behavior to GRB 180418A are GRB 051221A (Parsons et al. 2005b) and GRB 120804A (Lien et al. 2012; dark-yellow crosses and red diamonds, respectively, in Figure 7). Comparing the γ-ray properties (duration, hardness ratios, and fluence), redshifts, and host properties, we find that these bursts span the full range of short GRBs (Fong et al. 2015; Lien et al. 2016). Compared to the other two bursts, GRB 180418A has the longest duration, with $T_{90} \approx 1.9$ s, and is potentially one of the farthest ($z = 1$–2.25), although we note that the photometric redshift of GRB 120804A is $z \sim 1.3$ (Berger et al. 2013).

For the subset of 103 long GRBs that are similar in X-ray behavior to GRB 180418A, the main properties as determined by Swift/BAT are fairly heterogeneous. However, we find that five of these long GRBs (GRB 050416A, GRB 051016B, GRB 090927, GRB 100816A, and GRB 140710A; Cenko et al. 2005; Parsons et al. 2005a; Grupe et al. 2009; Oates et al. 2010;

Siegel et al. 2014, respectively)[30] have $T_{90} < 4$ s, while only 10 GRBs in the entire sample of 350 long GRBs have such durations. This means that half of the available population of long GRBs with $T_{90} \approx 2$–4 s shares X-ray afterglow luminosities and behavior similar to GRB 180418A. Like GRB 180418A, this subset falls 2.5σ below the long GRB median at early times and within 1σ of the median value at late times. To investigate the random chance of detecting long GRBs with $T_{90} < 4$ s, we draw 103 durations from the sample of 350 Swift long GRBs, 10,000 times. We find that in 9% of cases we obtain a sample containing five GRBs with $T_{90} < 4$ s. If we include GRB 180418A as part of this sample (making 6/11 of bursts with $T_{90} \leqslant 4$ s), this drops to 5%. Therefore, given the existing duration distribution, we cannot rule out the possibility that the observed statistics are based on random chance. However, the observed trends with X-ray luminosity are nonetheless intriguing, and a correlation between shorter durations and low X-ray luminosity may exist in the long GRB population. We note that these long GRBs are not necessarily the least luminous (Figure 7; Dereli et al. 2017) but represent those that track the X-ray behavior of GRB 180418A.

6. Discussion

6.1. GRB 180418A in the $E_{\gamma,peak,i}$–$E_{\gamma,iso}$ Relation

From our analysis of GRB 180418A in the context of the T_{90}–hardness plane, we found that the probability of GRB 180418A being short is 60% (Section 2.2) and that the low-density environment is more similar to those inferred for short GRBs. To further elucidate the nature of GRB 180418A, we compare the spectral properties of its prompt emission to those of short and long GRBs. Several studies (e.g., Amati et al. 2002, 2008; Yonetoku et al. 2004; Ghirlanda et al. 2015) have shown that the energy and luminosity of GRBs follow a correlation; in particular, we explore the correlation (the so-called "Amati relation"; Amati et al. 2002, 2008) between the $E_{\gamma,\rm iso}$ (1–10,000 keV range) and the intrinsic peak energy (i.e., the rest-frame peak energy, $E_{\gamma,\rm peak,i} = E_{\gamma,\rm peak}(1+z)$). Short and long GRBs track different positive correlations in the $E_{\gamma,\rm peak,i}$–$E_{\gamma,\rm iso}$ parameter space. Although the nature of this correlation is unclear, it may be connected to the different progenitor channels for both GRB populations, or potentially to viewing angle effects (if the angle between the jet axis and the line of sight of the observer is very small, the harder and brighter the γ-ray emission will be). The correlation followed by the short GRBs lies above and toward lower γ-ray energies than the one found for long GRBs, since the $E_{\gamma,\rm peak,i}$ of the short GRBs are generally higher than those of the long bursts (Figure 8).

In the case of GRB 180418A, we use our Fermi/GBM results (Section 2.2) to place the event in the $E_{\gamma,\rm peak,i}$–$E_{\gamma,\rm iso}$ plane. We find that GRB 180418A lies closer to the Amati correlation followed by the short GRB population (Minaev & Pozanenko 2020). Indeed, it falls within the space defined by this short GRB class in the $E_{\gamma,\rm peak,i}$–$E_{\gamma,\rm iso}$ plane and clearly falls off the correlation for long GRBs (Figure 8). In addition, no other long GRBs are consistent with the location of GRB 180418A. This comparison highlights the similarity in the prompt emission energetics between GRB 180418A and the short GRB population, pointing toward a possibly short GRB classification for GRB 180418A, and supporting our initial expectations. We also compare the $E_{\gamma,\rm peak,i}$ and $E_{\gamma,\rm iso}$ of GRB 180418A with the Swift low-luminosity long GRBs,[31] since they do not follow the canonical correlation of long GRBs (Dereli et al. 2017). We also highlight those GRBs of questionable classification (Figure 8): GRB 090426 (Antonelli et al. 2009; Levesque et al. 2010), with $T_{90} \approx 1.25$ s and similar prompt emission spectral properties, energy scales, and host properties to long GRBs, and GRB 100816A (D'Avanzo et al. 2014), with $T_{90} \approx 2.9$ s, one of the long GRBs with similar X-ray behavior to GRB 180418A (see Section 5) that was initially classified as a short GRB by Norris et al. (2010). We note that these events are not consistent with GRB 180418A within the errors and that GRB 180418A does not appear to be an ambiguous case in terms of its placement on the Amati relation in the short GRB class (Figure 8).

With the borderline γ-ray duration of GRB 180418A, it is also worth exploring how it compares to the proposed group of intermediate-duration GRBs. While the small group of intermediate-duration GRBs tends to populate the $E_{\gamma,\rm peak,i}$–$E_{\gamma,\rm iso}$ correlation of long GRBs (de Ugarte Postigo et al. 2011; Horváth et al. 2006), GRB 180418A does not clearly fall in this class. However, we note that some of the GRBs classified as intermediate-duration events by de Ugarte Postigo et al. (2011) have been later identified as short GRBs with extended emission (e.g., GRB 050724 and GRB 060614) or long GRBs with detected SNe (e.g., GRB 050416A and GRB 081007; Minaev & Pozanenko 2020).

6.2. GRB 180418A Environment and Reverse Shock

The detection of the afterglow of GRB 180418A enables us to investigate not only its burst properties but also its local and galactic environment. Our Gemini observations revealed a faint host galaxy for GRB 180418A at an angular offset of $\delta R = 0\farcs16 \pm 0\farcs04$. Although a secure redshift for GRB 180418A is not known, the inferred value of the GRB 180418A host luminosity, $L \approx 0.01$–$1L^*$ over the presumed redshift range of $z \approx 1$–2.25, is more consistent with the sub-L^* host galaxies of long GRBs (Savaglio et al. 2009; Blanchard et al. 2016) than the hosts of short GRBs, which are typically at 0.5–$3L^*$ (Berger 2014; Paterson et al. 2020). The angular offset translates to a projected physical distance of 1.29 ± 0.33 kpc at $z = 1$ (1.38 ± 0.34 kpc at $z = 1.5$). This places the burst at the lower end of the projected physical offset range for short GRBs, closer to its host than 90% of the known short GRBs (Fong & Berger 2013). Considering the long GRB population, which has smaller projected physical offsets, GRB 180418A falls at the median of the population (Blanchard et al. 2016). Given the proximity of the event to the host center, it is less expected, however, to find the low inferred circumburst density values that we do for GRB 180418A, $\approx 10^{-2}$ to 10^{-4} cm^{-3}, which are more consistent with the inferred values of short GRB circumburst environments. Since we are considering projected physical distances, there is still a possibility (since we are missing the depth component) for the real distance of GRB 180418A from the center of its host to be larger and,

[30] We note that GRB 050416A and GRB 090927 are clear cases of long GRBs since a supernova remnant was detected for GRB 050416A (Soderberg et al. 2007) and GRB 090927 is most likely a collapsar (Nicuesa Guelbenzu et al. 2012).

[31] We note that $E_{\gamma,\rm peak,i}$ and $E_{\gamma,\rm iso}$ of GRB 140710A are not available in the literature.

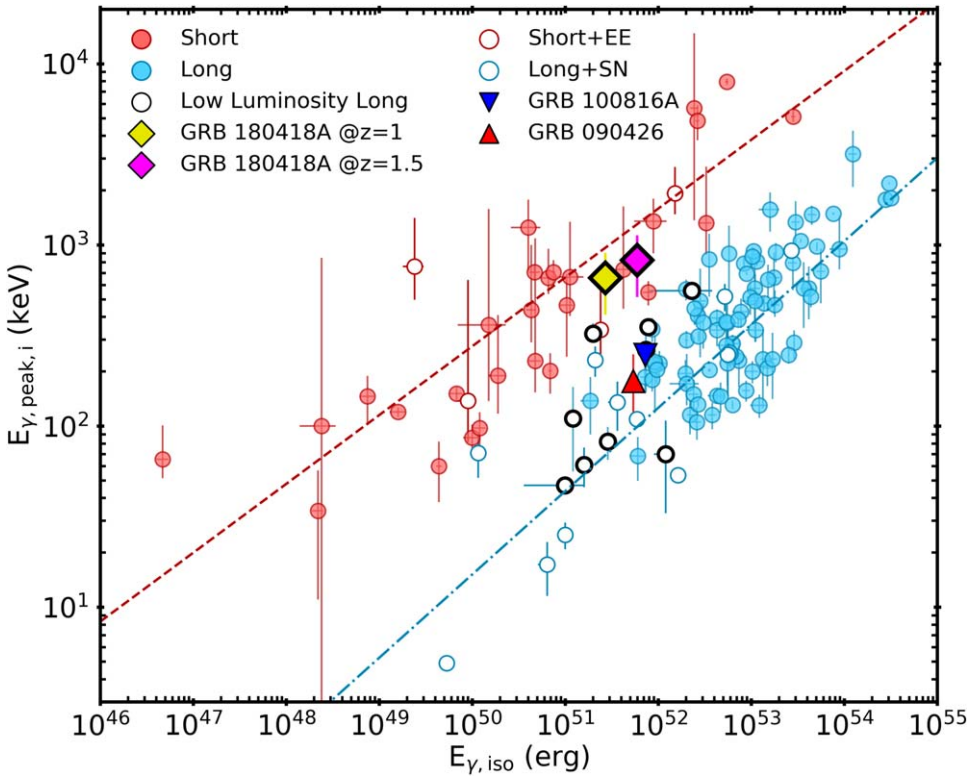

Figure 8. $E_{\gamma,\mathrm{peak,i}}$–$E_{\gamma,\mathrm{iso}}$ relation for Swift and Fermi short (light red circles) and long (blue circles) GRBs (Minaev & Pozanenko 2020), along with GRB 180418A (diamonds) at $z = 1$ and 1.5. We highlight short GRBs with extended emission (red open circles) and long GRBs with detected SNe (blue open circles). GRB 180418A is fully consistent with the short GRB population in the $E_{\gamma,\mathrm{peak,i}}$–$E_{\gamma,\mathrm{iso}}$ plane and is a clear outlier compared to the space occupied by long GRBs (and the Amati correlation). Best-fit correlation models are indicated with lines (red dashed line for short GRBs and blue dashed–dotted line for long GRBs; Minaev & Pozanenko 2020). We also highlight the ambiguous cases of GRB 090426 (red triangle; Antonelli et al. 2009) and GRB 100816A (D'Avanzo et al. 2014 blue triangle; see Section 6.1) and the low-luminosity long GRBs (circles with black borders; Dereli et al. 2017).

therefore, explaining the low-density values inferred for this event.

We note that for six long GRBs with clearly detected RSs (GRB 990123, GRB 130427A, GRB 160509A, GRB 161219B, GRB 160625B, and GRB 181201A; Mészáros & Rees 1999; Laskar et al. 2013, 2016, 2018; Alexander et al. 2017; Laskar et al. 2019) the circumburst densities are very low, $\approx 5 \times 10^{-5}$ cm^{-3} to 10^{-2} cm^{-3} (Laskar et al. 2018). In the case of short GRBs, there are three events for which radio detections of RSs have been claimed: GRB 051221A (Soderberg et al. 2006), GRB 160821B (Lamb et al. 2019; Troja et al. 2019), and potentially GRB 200522A (Fong et al. 2021). For these events, the inferred circumburst densities are low although more consistent with average short GRBs, ranging between $\approx 10^{-4}$ and 10^{-2} cm^{-3}. In this framework, it is thought that these low-density environments, for both long and short GRBs, may be responsible for a slow-cooling RS, which allows the RS emission to be detectable for longer (Chevalier et al. 2004; Laskar et al. 2013). In the case of GRB 180418A, the circumburst values we inferred (Table 3) are in agreement with those seen in the RS scenario.

Including RS emission potentially explains the excess in the early-time ($\delta t \approx 1$ day) afterglow emission of GRB 180418A (Becerra et al. 2019; and this paper). If GRB 180418A is indeed a short GRB, then it will be the first with an RS detected in the optical band and with self-consistent RS model parameters ($\Gamma_0 \gtrsim 150$ and $R_\mathrm{B} \approx 5.2$; Section 4.3). The other short GRB with reported values of the initial bulk Lorentz factor and magnetization parameter is GRB 160821B (Lamb et al. 2019); however, Lamb et al. (2019) inferred these values from the FS parameters instead of using the information from the RS spectral parameters as we do in our work. In the case of GRB 051221A and GRB 200522A, the jet Lorentz factors are in the range of 18–26 and $\gtrsim$10, respectively (Soderberg et al. 2006; Fong et al. 2021), but in both studies, assumptions on the magnetization parameter were made. On the other hand, comparing the GRB 180418A RS parameters with those of the long GRBs ($\Gamma_0 \approx 100$–300 and $R_\mathrm{B} \approx 0.5$–10; Laskar et al. 2018), we find that the values for GRB 180418A are encompassed by the ranges of the initial jet Lorentz factor and magnetization parameter of long GRBs.

6.3. GRB 180418A and Jet Opening Angles

Finally, we compare the cumulative distributions of the minimum values for opening angles of GRB 180418A with those for the opening angles corresponding to the short and long GRB populations (see Figure 9). From a progenitor standpoint, the massive star progenitors of long GRBs provide a natural collimating medium prior to jet breakout (Mészáros & Rees 2001; Zhang et al. 2003). In contrast, BNS and neutron star–black hole (NS–BH) mergers have no clear analogous mechanism to maintain jet collimation beyond the jet's breakout from the kilonova ejecta. Based on jet predictions of simulations of post-merger black hole accretion (Ruffert & Janka 1999; Aloy et al. 2005; Rezzolla et al. 2011), the general expectation is that short GRBs can achieve wider jet opening angles. The wider jets, coupled with their circumburst density environments, which are orders of magnitude lower than long

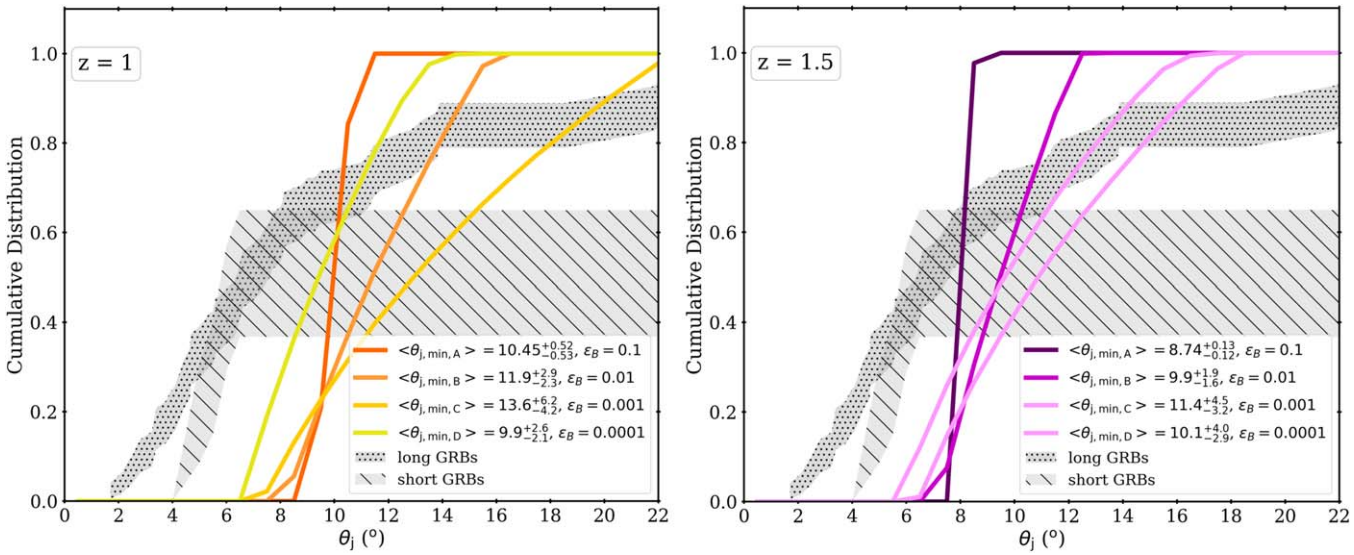

Figure 9. Cumulative distributions of the minimum values of the jet opening angles (θ_j) at $z = 1$ (left) and $z = 1.5$ (right) for GRB 180418A. The different colors correspond to the different cases shown in Table 3. The cumulative distributions of the opening angles for short and long GRBs are shown in the dashed light-gray and dotted dark-gray areas, respectively. In this case, we have applied survival statistics for right-censored data to account for the lower limits of the opening angles in both populations. The plotted areas correspond to their 68% confidence intervals.

GRBs (Fong et al. 2015), lead to later expected break times (see Equation (2)). Taken together, these characteristics present an observational challenge in detecting signatures of the expected wider jets in short GRBs. Indeed, our knowledge of short GRB jets generally comes from a few measurements with $\theta_j \approx 6°$ (Fong et al. 2015).

With the nondetection of a jet break to ≈ 38.5 days in the X-ray afterglow of GRB 180418A, we infer an opening angle constraint of $\theta_j \gtrsim 9°$–$14°$ (Figure 9), depending on the value of the redshift, microphysical parameters, and explosion properties. For instance, from the best-fit multiwavelength model, we find $\theta_j \gtrsim 17.^{\circ}3\zeta^{1/2}$. This limit constrains the jet of GRB 180418A to be relatively wide in the context of the distribution of long GRBs, which have a median opening angle of $\theta_j \approx 7°$ (Figure 9; Frail et al. 2001; Bloom et al. 2003; Goldstein et al. 2016), and $\approx 75\%$ of which have $\theta_j \lesssim 10°$. Instead, the opening angle constraint of GRB 180418A is more consistent with the short GRB distribution, which only consists of six jet measurements and several lower limits to date with $\langle\theta_j\rangle = 16° \pm 10°$ (Fong et al. 2015). GRB 180418A increases the small sample of GRBs with wide opening angle constraints, in particular, GRB050724A with $\theta_j \gtrsim 25°$ (Berger et al. 2005), GRB 120804A with $\theta_j \gtrsim 13°$ (Berger et al. 2013; Fong et al. 2015), and GRB 150101B with $\theta_j \gtrsim 9°$ (Fong et al. 2016), all inferred from late-time X-ray observations.

We can also use the opening angle to calculate the *lower* limit on the beaming-corrected, true energy scale of GRB 180418A to be $E_{\rm true,tot} \equiv E_K + E_\gamma \gtrsim (1.97 - 44) \times 10^{50}$ erg at $z = 1$ and $E_{\rm true,tot} \gtrsim (2.68 - 57) \times 10^{50}$ erg at $z = 1.5$, with the corresponding upper limits set by the isotropic-equivalent total energies of $E_{\rm iso,tot} = (1.2 - 29) \times 10^{52}$ erg and $E_{\rm iso,tot} = (2.2 - 36) \times 10^{52}$ erg. The mechanisms that power the relativistic jet (Shibata & Hotokezaka 2019), either the thermal energy that is released during the $\nu\bar{\nu}$ annihilation process in baryonic outflows (Jaroszynski 1993; Mochkovitch et al. 1993) or magnetohydrodynamic processes in the accretion remnant of a black hole (e.g., Blandford & Znajek 1977; Rosswog et al. 2003; Ruiz et al. 2016; Siegel & Metzger 2017), are expected to attain different energy releases. In particular, it is expected that the released energy from the $\nu\bar{\nu}$ annihilation mechanism reaches levels of 10^{48}–10^{49} erg (Birkl et al. 2007), with larger energy scales of $> 10^{50}$ erg for magnetized jets (e.g., Blandford & Znajek 1977; Rosswog et al. 2003; Ruiz et al. 2016; Siegel & Metzger 2017). In addition, theoretical studies have shown that there are different jet opening angle predictions based on the magnetization of the jet (Rosswog & Ramirez-Ruiz 2002; Duffell et al. 2018; Nathanail et al. 2020), as well as different outcomes for BNS and NS–BH mergers (Murguia-Berthier et al. 2017), with more magnetized outflows found to produce wider jets with $\theta_j \gtrsim 10°$ (Nathanail et al. 2020).

7. Conclusions

In this paper we present the multiwavelength monitoring campaign on the afterglow of the possibly short GRB 180418A and the discovery of its faint host galaxy. In particular, the superb angular resolution of Chandra allowed us to disentangle a contaminating source in the Swift/XRT aperture and track the afterglow to $\delta t \approx 38.5$ days. Our main conclusions are summarized as follows:

1. In terms of traditional classification schemes such as the T_{90}–hardness plane and the Amati relations, we find that GRB 180418A is more likely a short GRB. In the context of the Fermi/GBM population, we find a probability of being short (from the T_{90}–hardness plane) of 60% and consistency within the population of short GRBs in the Amati relation.
2. The detection of the X-ray afterglow at $\delta t \approx 38.5$ days makes this burst one of the very few short GRBs with a late-time detection in X-rays ($\gtrsim$20 days).
3. The X-ray afterglow light curve, coupled with the optical multiband detections, exhibits a single power-law decline. We calculate the lower limit of its jet opening angle to be $\theta_j \gtrsim 9°$–$14°$ (assuming $z = 1$–1.5). These lower limits reveal a moderately wide jet angle that is consistent with the distribution of angles for short GRB jets and the expectations for BNS/NS–BH merger relativistic outflows.

4. When comparing the X-ray afterglow luminosity of GRB 180418A with those of the short and long GRBs detected by Swift/BAT, we find that only two short GRBs track the behavior of GRB 180418A. We also notice that half of the available population of long GRBs with $T_{90} \approx 2$–4 s shows X-ray afterglow luminosities and behavior similar to GRB 180418A.
5. Modeling the afterglow with a joint synchrotron FS and RS, we find beaming-corrected energy scales of $E_{\rm true,tot} \gtrsim (1.97\text{–}44) \times 10^{50}$ erg and $E_{\rm true,tot} \gtrsim (2.68\text{–}57) \times 10^{50}$ erg and circumburst densities of $n_0 = (2.56\text{–}110) \times 10^{-4}$ cm^{-3} and $n_0 = (2.21\text{–}160) \times 10^{-4}$ cm^{-3} at $z = 1$ and $z = 1.5$, respectively. The low inferred circumburst density is also consistent with both short and long GRBs with detected RSs.
6. GRB 180418A is the first short GRB with an RS detected in the optical band with self-consistent RS model parameters.
7. We find a faint host galaxy coincident with the Chandra X-ray and optical afterglow positions. The featureless afterglow and host spectrum, coupled with the detection of the afterglow with UVOT, constrain the redshift range of the burst to most likely be $z \approx 1$–2.25.

The continuous coverage in the optical and the late-time detections in X-rays, coupled with the nature of GRB 180418A, make this event an exceptional GRB case. Our work demonstrates that multiwavelength afterglow observations are essential not only at early times following the GRB trigger (detection of RS in the optical; Becerra et al. 2019) but also at late times (better constraints of the jet opening angle). The power of ToO multiwavelength campaigns is vital for further investigating the increasingly diverse behavior of GRB afterglows, determining the energetics and environments where bursts occur, and studying the potential GRB central engine and progenitor channels. More deep follow-up observations are necessary and encouraged to increase the number of detected jet breaks in future short GRB afterglows.

The authors acknowledge Phil Evans for the useful advice to obtain the full set of X-ray GRB afterglow light curves from the UK Swift Science Data Centre. The authors thank Daniel Perley for his valuable contribution to proposals.

The Fong Group at Northwestern acknowledges support by the National Science Foundation under grant Nos. AST-1814782 and AST-1909358. Support for this work was provided by the National Aeronautics and Space Administration through Chandra award No. G08-19025X issued by the Chandra X-ray Center, which is operated by the Smithsonian Astrophysical Observatory for and on behalf of the National Aeronautics Space Administration under contract NAS8-03060. P.V. acknowledges support from NASA grants 80NSSC19K0595 and NNM11AA01A.

This work made use of data supplied by the UK Swift Science Data Centre at the University of Leicester.

Based on observations obtained at the international Gemini Observatory (Program IDs GS-2018A-Q-127, GN-2018A-Q-121, GN-2018B-Q-117), a program of NOIRLab, which is managed by the Association of Universities for Research in Astronomy (AURA) under a cooperative agreement with the National Science Foundation on behalf of the Gemini Observatory partnership: the National Science Foundation (United States), National Research Council (Canada), Agencia Nacional de Investigación y Desarrollo (Chile), Ministerio de Ciencia, Tecnología e Innovación (Argentina), Ministério da Ciência, Tecnologia, Inovações e Comunicações (Brazil), and Korea Astronomy and Space Science Institute (Republic of Korea).

This work was enabled by observations made from the Gemini-North telescope, located within the Maunakea Science Reserve and adjacent to the summit of Maunakea. We are grateful for the privilege of observing the universe from a place that is unique in both its astronomical quality and its cultural significance.

Observations reported in this paper were obtained at the MMT Observatory, a joint facility of the University of Arizona and the Smithsonian Institution (Programs 2018C-UAO-G4, UAO-G213-20A, UAO-G4, UAO-G7, UAO-G212-20A, 2018b-UAO-G15). MMT Observatory access was supported by Northwestern University and the Center for Interdisciplinary Exploration and Research in Astrophysics (CIERA).

Observations obtained by the United Kingdom Infrared Telescope (UKIRT; program: U/18A/UA01) were supported by NASA and operated under an agreement among the University of Hawaii, the University of Arizona, and Lockheed Martin Advanced Technology Center; operations are enabled through the cooperation of the East Asian Observatory. We thank the Cambridge Astronomical Survey Unit (CASU) for processing the WFCAM data and the WFCAM Science Archive (WSA) for making the data available.

Facilities: FERMI/GBM, Swift(BAT and XRT), Chandra (ACIS-S), Gemini-S and -N(GMOS), UKIRT(WFCAM), MMT(MMIRS and Binospec).

Software: `IRAF` (Tody & Crawford 1986; Tody et al. 1993), `SExtractor` (Bertin & Arnouts 1996), `CIAO` software package (v.4.12 Fruscione et al. 2006), `HEASoft` software (v.6.17; Blackburn et al. 1999; NASA High Energy Astrophysics Science Archive Research Center (HEASARC), 2014), `HOTPANTS` (Becker 2015), `mclust` (Scrucca et al. 2016), `XSPEC` (Arnaud 1996), `lifelines` (Davidson-Pilon et al. 2020).

ORCID iDs

W. Fong https://orcid.org/0000-0002-7374-935X
P. Veres https://orcid.org/0000-0002-2149-9846
T. Laskar https://orcid.org/0000-0003-1792-2338
K. Paterson https://orcid.org/0000-0001-8340-3486
M. Lally https://orcid.org/0000-0002-4443-6725
A. E. Nugent https://orcid.org/0000-0002-2028-9329
N. R. Tanvir https://orcid.org/0000-0003-3274-6336
D. Cornish https://orcid.org/0000-0002-1533-9037
E. Berger https://orcid.org/0000-0002-9392-9681
Nathan Smith https://orcid.org/0000-0001-5510-2424

References

Abbott, B. P., Abbott, R., Abbott, T. D., et al. 2017, ApJL, 848, L13
Ackermann, M., Ajello, M., Asano, K., et al. 2011, ApJ, 729, 114
Alexander, K. D., Laskar, T., Berger, E., et al. 2017, ApJ, 848, 69
Aloy, M. A., Janka, H. T., & Müller, E. 2005, A&A, 436, 273
Amati, L., Frontera, F., Tavani, M., et al. 2002, A&A, 390, 81
Amati, L., Guidorzi, C., Frontera, F., et al. 2008, MNRAS, 391, 577
Antonelli, L. A., D'Avanzo, P., Perna, R., et al. 2009, A&A, 507, L45
Arnaud, K. A. 1996, in ASP Conf. Ser. 101, XSPEC: The First Ten Years, ed. G. H. Jacoby & J. Barnes (San Francisco, CA: ASP), 17

Astropy Collaboration, Robitaille, T. P., Tollerud, E. J., et al. 2013, A&A, 558, A33
Barthelmy, S. D., Barbier, L. M., Cummings, J. R., et al. 2005, SSRv, 120, 143
Barthelmy, S. D., Baumgartner, W. H., Cummings, J. R., et al. 2009, GCN, 9494, 1
Becerra, R. L., Dichiara, S., Watson, A. M., et al. 2019, ApJ, 881, 12
Becker, A. 2015, HOTPANTS: High Order Transform of PSF ANd Template Subtraction, Astrophysics Source Code Library, ascl:1504.004
Belczynski, K., Holz, D. E., Fryer, C. L., et al. 2010, ApJ, 708, 117
Bennett, C. L., Larson, D., Weiland, J. L., & Hinshaw, G. 2014, ApJ, 794, 135
Berger, E. 2014, ARA&A, 52, 43
Berger, E., Kulkarni, S. R., Frail, D. A., & Soderberg, A. M. 2003, ApJ, 599, 408
Berger, E., Price, P. A., Cenko, S. B., et al. 2005, Natur, 438, 988
Berger, E., Zauderer, B. A., Chary, R. R., et al. 2014, ApJ, 796, 96
Berger, E., Zauderer, B. A., Levan, A., et al. 2013, ApJ, 765, 121
Bernardini, M. G., Margutti, R., Mao, J., Zaninoni, E., & Chincarini, G. 2012, A&A, 539, A3
Bertin, E., & Arnouts, S. 1996, A&AS, 117, 393
Bhat, N. P., Meegan, C. A., von Kienlin, A., et al. 2016, ApJS, 223, 28
Birkl, R., Aloy, M. A., Janka, H. T., & Müller, E. 2007, A&A, 463, 51
Bissaldi, E., & Veres, P. 2018, GCN, 22656, 1
Blackburn, J. K., Shaw, R. A., Payne, H. E., Hayes, J. J. E., & Heasarc 1999, FTOOLS: A General Package of Software to Manipulate FITS Files, Astrophysics Source Code Library, ascl:9912.002
Blanchard, P. K., Berger, E., & Fong, W.-f. 2016, ApJ, 817, 144
Blandford, R. D., & Znajek, R. L. 1977, MNRAS, 179, 433
Bloom, J. S., Frail, D. A., & Kulkarni, S. R. 2003, ApJ, 594, 674
Bloom, J. S., Kulkarni, S. R., & Djorgovski, S. G. 2002a, AJ, 123, 1111
Bloom, J. S., Kulkarni, S. R., Price, P. A., et al. 2002b, ApJL, 572, L45
Bright, J., Mooley, K. P., & Fender, R. P. 2018, GCN, 22697, 1
Bromberg, O., Nakar, E., Piran, T., & Sari, R. 2013, ApJ, 764, 179
Burrows, D. N., Grupe, D., Capalbi, M., et al. 2006, ApJ, 653, 468
Burrows, D. N., Hill, J. E., Nousek, J. A., et al. 2005, SSRv, 120, 165
Casali, M., Adamson, A., Alves de Oliveira, C., et al. 2007, A&A, 467, 777
Cenko, S. B., Kulkarni, S. R., Gal-Yam, A., & Berger, E. 2005, GCN, 3542, 1
Chevalier, R. A., Li, Z.-Y., & Fransson, C. 2004, ApJ, 606, 369
Choi, C., Kim, Y., Park, W., Shin, S., & Im, M. 2018, GCN, 22668, 1
Clocchiatti, A., Suntzeff, N. B., Covarrubias, R., & Candia, P. 2011, AJ, 141, 163
Craig, M., Crawford, S., Seifert, M., et al. 2017, astropy/ccdproc: v1.3.0.post1, Zenodo, doi:10.5281/zenodo.1069648
Cucchiara, A., Levan, A. J., Fox, D. B., et al. 2011, ApJ, 736, 7
D'Avanzo, P., Salvaterra, R., Bernardini, M. G., et al. 2014, MNRAS, 442, 2342
D'Elia, V., D'Ai, A., Evans, P. A., et al. 2018, GCN, 22646, 1
Davidson-Pilon, C., Kalderstam, J., Jacobson, N., et al. 2020, CamDavidsonPilon/lifelines: v0.24.16, Zenodo, doi:10.5281/zenodo.3937749
de Jager, O. C., & Harding, A. K. 1992, ApJ, 396, 161
de Ugarte Postigo, A., Horváth, I., Veres, P., et al. 2011, A&A, 525, A109
Del Vecchio, R., Dainotti, M. G., & Ostrowski, M. 2016, ApJ, 828, 36
Della Valle, M., Chincarini, G., Panagia, N., et al. 2006, Natur, 444, 1050
Dereli, H., Boër, M., Gendre, B., et al. 2017, ApJ, 850, 117
Dezalay, J. P., Barat, C., Talon, R., et al. 1992, in AIP Conf. Ser. 265, Gamma-Ray Bursts, ed. W. S. Paciesas & G. J. Fishman (New York: AIP), 304
Dorman, B., Arnaud, K. A., & Gordon, C. A. 2003, BAAS, 35, 641
Duffell, P. C., Quataert, E., Kasen, D., & Klion, H. 2018, ApJ, 866, 3
Evans, P. A., Beardmore, A. P., Page, K. L., et al. 2007, A&A, 469, 379
Evans, P. A., Beardmore, A. P., Page, K. L., et al. 2009, MNRAS, 397, 1177
Fong, W., & Berger, E. 2013, ApJ, 776, 18
Fong, W., Berger, E., Chornock, R., et al. 2013, ApJ, 769, 56
Fong, W., Berger, E., Margutti, R., et al. 2012, ApJ, 756, 189
Fong, W., Berger, E., Margutti, R., & Zauderer, B. A. 2015, ApJ, 815, 102
Fong, W., Laskar, T., Rastinejad, J., et al. 2021, ApJ, 906, 127
Fong, W., Margutti, R., Chornock, R., et al. 2016, ApJ, 833, 151
Fong, W., Tanvir, N. R., Levan, A. J., & Chornock, R. 2018, GCN, 22659, 1
Frail, D. A., Kulkarni, S. R., Sari, R., et al. 2001, ApJL, 562, L55
Fruchter, A. S., Levan, A. J., Strolger, L., et al. 2006, Natur, 441, 463
Fruscione, A., McDowell, J. C., Allen, G. E., et al. 2006, Proc. SPIE, 6270, 62701V
Fynbo, J. P. U., Watson, D., Thöne, C. C., et al. 2006, Natur, 444, 1047
Galama, T. J., Vreeswijk, P. M., van Paradijs, J., et al. 1998, Natur, 395, 670
Garmire, G. P., Bautz, M. W., Ford, P. G., & Nousek, J. A. 2003, Proc. SPIE, 4851, 28
Gehrels, N. 1986, ApJ, 303, 336
Gehrels, N., Barthelmy, S. D., Burrows, D. N., et al. 2008, ApJ, 689, 1161
Gehrels, N., Chincarini, G., Giommi, P., et al. 2004, ApJ, 611, 1005
Ghirlanda, G., Bernardini, M. G., Calderone, G., & D'Avanzo, P. 2015, JHEAp, 7, 81
GLAST Facility Science Team, Gehrels, N., & Michelson, P. 1999, APh, 11, 277
Goad, M. R., Osborne, J. P., Beardmore, A. P., & Evans, P. A. 2018, GCN, 22650, 1
Goldstein, A., Connaughton, V., Briggs, M. S., & Burns, E. 2016, ApJ, 818, 18
Goldstein, A., Veres, P., Burns, E., et al. 2017, ApJL, 848, L14
Granot, J., & Piran, T. 2012, MNRAS, 421, 570
Granot, J., & Sari, R. 2002, ApJ, 568, 820
Gruber, D., Goldstein, A., Weller von Ahlefeld, V., et al. 2014, ApJS, 211, 12
Grupe, D., Cummings, J. R., Gronwall, C., et al. 2009, GCN, 9945, 1
Guidorzi, C., Martone, R., Kobayashi, S., et al. 2018, GCN, 22648, 1
Hamly, N. C., Collins, R. S., Cross, N. J. G., et al. 2008, MNRAS, 384, 637
HI4PI Collaboration, Ben Bekhti, N., Flöer, L., et al. 2016, A&A, 594, A116
Hjorth, J., & Bloom, J. S. 2012, in Gamma-Ray Bursts, ed. C. Kouveliotou et al. (Cambridge: Cambridge Univ. Press), 169
Horiuchi, T., Hanayama, H., Honma, M., et al. 2018, GCN, 22670, 1
Horváth, I., Balázs, L. G., Bagoly, Z., Ryde, F., & Mészáros, A. 2006, A&A, 447, 23
Jaroszynski, M. 1993, AcA, 43, 183
Jespersen, C. K., Severin, J. B., Steinhardt, C. L., et al. 2020, ApJL, 896, L20
Jin, Z.-P., Li, X., Wang, H., et al. 2018, ApJ, 857, 128
Kann, D. A., Klose, S., Zhang, B., et al. 2010, ApJ, 720, 1513
Kobayashi, S. 2000, ApJ, 545, 807
Kobayashi, S., & Sari, R. 2000, ApJ, 542, 819
Kouveliotou, C., Meegan, C. A., Fishman, G. J., et al. 1993, ApJL, 413, L101
Kulkarni, S., & Desai, S. 2017, Ap&SS, 362, 70
Lamb, G. P., Tanvir, N. R., Levan, A. J., et al. 2019, ApJ, 883, 48
Laskar, T., Alexander, K. D., Berger, E., et al. 2016, ApJ, 833, 88
Laskar, T., Alexander, K. D., Berger, E., et al. 2018, ApJ, 862, 94
Laskar, T., Alexander, K. D., Gill, R., et al. 2019, ApJL, 878, L26
Laskar, T., Berger, E., Tanvir, N., et al. 2014, ApJ, 781, 1
Laskar, T., Berger, E., Zauderer, B. A., et al. 2013, ApJ, 776, 119
Laskar, T., van Eerten, H., Schady, P., et al. 2019, ApJ, 884, 121
Levan, A. J., Jakobsson, P., Hurkett, C., et al. 2007, MNRAS, 378, 1439
Levesque, E. M., Bloom, J. S., Butler, N. R., et al. 2010, MNRAS, 401, 963
Lien, A., Sakamoto, T., Barthelmy, S. D., et al. 2016, ApJ, 829, 7
Lien, A. Y., Barthelmy, S. D., Baumgartner, W. H., et al. 2012, GCN, 13573, 1
Lloyd-Ronning, N. 2018, Galax, 6, 103
Malesani, D., Heintz, K. E., Stone, M., & Stone, J. 2018, GCN, 22660, 1
Mandhai, S., Tanvir, N., Lamb, G., Levan, A., & Tsang, D. 2018, Galax, 6, 130
Markwardt, C. B., Barthelmy, S. D., Cummings, J. R., et al. 2020, GCN, 28658, 1
Mazets, E. P., Golenetskii, S. V., Ilinskii, V. N., et al. 1981, Ap&SS, 80, 3
Meegan, C., Lichti, G., Bhat, P. N., et al. 2009, ApJ, 702, 791
Meszaros, P., & Rees, M. J. 1992, MNRAS, 257, 29P
Meszaros, P., & Rees, M. J. 1993, ApJL, 418, L59
Mészáros, P., & Rees, M. J. 1999, MNRAS, 306, L39
Mészáros, P., & Rees, M. J. 2001, ApJL, 556, L37
Minaev, P. Y., & Pozanenko, A. S. 2020, MNRAS, 492, 1919
Misra, K., Paswan, A., Singh, M., et al. 2018, GCN, 22663, 1
Mochkovitch, R., Hernanz, M., Isern, J., & Martin, X. 1993, Natur, 361, 236
Murguia-Berthier, A., Ramirez-Ruiz, E., Montes, G., et al. 2017, ApJL, 835, L34
Nakar, E. 2007, PhR, 442, 166
NASA High Energy Astrophysics Science Archive Research Center (HEASARC) 2014, HEAsoft: Unified Release of FTOOLS and XANADU, Astrophysics Source Code Library, ascl:1408.004
Nathanail, A., Gill, R., Porth, O., Fromm, C. M., & Rezzolla, L. 2020, MNRAS, 495, 3780
Nicuesa Guelbenzu, A., Klose, S., Greiner, J., et al. 2012, A&A, 548, A101
Norris, J., Ukwatta, T. N., Barthelmy, S. D., et al. 2010, GCN, 11113, 1
Norris, J. P., Cline, T. L., Desai, U. D., & Teegarden, B. J. 1984, Natur, 308, 434
Nysewander, M., Fruchter, A. S., & Pe'er, A. 2009, ApJ, 701, 824
Oates, S. R., Barthelmy, S. D., Beardmore, A. P., et al. 2010, GCN, 11102, 1
Palmer, D. M., Barthelmy, S. D., Cummings, J. R., et al. 2018, GCN, 22658, 1
Panaitescu, A. 2005, MNRAS, 362, 921
Panaitescu, A., & Kumar, P. 2002, ApJ, 571, 779
Parsons, A., Barthelmy, S., Beardmore, A., et al. 2005a, GCN, 4103, 1
Parsons, A., Barthelmy, S., Burrows, D., et al. 2005b, GCN, 4363, 1
Paterson, K., Fong, W., Nugent, A., et al. 2020, ApJL, 898, L32
Perley, D. A., Cenko, S. B., Corsi, A., et al. 2014, ApJ, 781, 37

Piran, T. 1995, arXiv:astro-ph/9507114
Piran, T. 1999, PhR, 314, 575
Piran, T. 2005, RvMP, 76, 1143
Plucinsky, P. P., Beardmore, A. P., Foster, A., et al. 2017, A&A, 597, A35
Price-Whelan, A. M., Sipőcz, B. M., Günther, H. M., et al. 2018, AJ, 156, 123
Racusin, J. L., Liang, E. W., Burrows, D. N., et al. 2009, ApJ, 698, 43
Rees, M. J., & Meszaros, P. 1992, MNRAS, 258, 41
Rezzolla, L., Giacomazzo, B., Baiotti, L., et al. 2011, ApJL, 732, L6
Rhoads, J. E. 1997, ApJL, 487, L1
Rhoads, J. E. 1999, ApJ, 525, 737
Roming, P. W. A., Kennedy, T. E., Mason, K. O., et al. 2005, SSRv, 120, 95
Rosswog, S., & Ramirez-Ruiz, E. 2002, MNRAS, 336, L7
Rosswog, S., Ramirez-Ruiz, E., & Davies, M. B. 2003, MNRAS, 345, 1077
Ruffert, M., & Janka, H. T. 1999, A&A, 344, 573
Ruiz, M., Lang, R. N., Paschalidis, V., & Shapiro, S. L. 2016, ApJL, 824, L6
Ryan, G., van Eerten, H., MacFadyen, A., & Zhang, B.-B. 2015, ApJ, 799, 3
Sakamoto, T., Barthelmy, S. D., Baumgartner, W. H., et al. 2011, ApJS, 195, 2
Salvaterra, R. 2015, JHEAp, 7, 35
Sari, R., & Piran, T. 1995, ApJL, 455, L143
Sari, R., Piran, T., & Halpern, J. P. 1999, ApJL, 519, L17
Sari, R., Piran, T., & Narayan, R. 1998, ApJL, 497, L17
Savaglio, S., Glazebrook, K., & Le Borgne, D. 2009, ApJ, 691, 182
Savchenko, V., Ferrigno, C., Kuulkers, E., et al. 2017, ApJL, 848, L15
Schady, P. 2018, GCN, 22662, 1
Schady, P., & Chen, T. W. 2018, GCN, 22666, 1
Schlafly, E. F., & Finkbeiner, D. P. 2011, ApJ, 737, 103
Schulze, S., Klose, S., Björnsson, G., et al. 2011, A&A, 526, A23
Scrucca, L., Fop, M., Murphy, T. B., & Raftery, A. E. 2016, R J., 8, 205
Sedov, L. I. 1959, Similarity and Dimensional Methods in Mechanics (Amsterdam: Elsevier)
Selsing, J., Krühler, T., Malesani, D., et al. 2018, A&A, 616, A48
Shibata, M., & Hotokezaka, K. 2019, ARNPS, 69, 41
Siegel, D. M., & Metzger, B. D. 2017, PhRvL, 119, 231102
Siegel, M. H., Burrows, D. N., Chester, M. M., et al. 2014, GCN, 16563, 1
Siegel, M. H., & D'Elia, V. 2018, GCN, 22665, 1
Sironi, L., & Giannios, D. 2013, ApJ, 778, 107
Sironi, L., & Spitkovsky, A. 2011, ApJ, 726, 75
Soderberg, A. M., Berger, E., Kasliwal, M., et al. 2006, ApJ, 650, 261
Soderberg, A. M., Nakar, E., Cenko, S. B., et al. 2007, ApJ, 661, 982
Sota, A., Hu, Y., Tello, J. C., Carrasco, I., & Castro-Tirado, A. J. 2018, GCN, 22657, 1
Tanvir, N. R., Fox, D. B., Levan, A. J., et al. 2009, Natur, 461, 1254
Taylor, G. 1950, RSPSA, 201, 159
Tody, D. 1986, Proc. SPIE, 627, 733
Tody, D. 1993, in ASP Conf. Ser. 52, Astronomical Data Analysis Software and Systems II, ed. R. J. Hanisch, R. J. V. Brissenden, & J. Barnes (San Francisco, CA: ASP), 173
Tomczak, A. R., Quadri, R. F., Tran, K.-V. H., et al. 2014, ApJ, 783, 85
Troja, E., Castro-Tirado, A. J., Becerra González, J., et al. 2019, MNRAS, 489, 2104
Troja, E., Sakamoto, T., Cenko, S. B., et al. 2016, ApJ, 827, 102
van Eerten, H., & MacFadyen, A. 2013, ApJ, 767, 141
van Eerten, H. J., Leventis, K., Meliani, Z., Wijers, R. A. M. J., & Keppens, R. 2010, MNRAS, 403, 300
van Paradijs, J., Kouveliotou, C., & Wijers, R. A. M. J. 2000, ARA&A, 38, 379
Verner, D. A., Ferland, G. J., Korista, K. T., & Yakovlev, D. G. 1996, ApJ, 465, 487
von Kienlin, A., Meegan, C. A., Paciesas, W. S., et al. 2020, ApJ, 893, 46
Wachter, K., Leach, R., & Kellogg, E. 1979, ApJ, 230, 274
Wainwright, C., Berger, E., & Penprase, B. E. 2007, ApJ, 657, 367
Wilms, J., Allen, A., & McCray, R. 2000, ApJ, 542, 914
Woosley, S. E., & Bloom, J. S. 2006, ARA&A, 44, 507
Xin, L. P., Yan, J. Z., Wei, J. Y., et al. 2018, GCN, 22661, 1
Yonetoku, D., Murakami, T., Nakamura, T., et al. 2004, ApJ, 609, 935
Yost, S. A., Harrison, F. A., Sari, R., & Frail, D. A. 2003, ApJ, 597, 459
Zhang, B., & Kobayashi, S. 2005, ApJ, 628, 315
Zhang, W., Woosley, S. E., & MacFadyen, A. I. 2003, ApJ, 586, 356
Zheng, W., & Filippenko, A. V. 2018, GCN, 22647, 1
Zou, Y. C., Wu, X. F., & Dai, Z. G. 2005, MNRAS, 363, 93
Zwart, J. T. L., Barker, R. W., Biddulph, P., et al. 2008, MNRAS, 391, 1545